



# Slow Resting State Fluctuations Enhance Neuronal and Behavioral Responses to Looming Sounds

B. Sancristóbal<sup>1,2,7</sup> · F. Ferri<sup>3</sup> · A. Longtin<sup>1,4</sup> · M. G. Perrucci<sup>3</sup> · G. L. Romani<sup>3</sup> · G. Northoff<sup>2,4,5,6</sup>

Received: 15 September 2020 / Accepted: 17 February 2021

© The Author(s), under exclusive licence to Springer Science+Business Media, LLC, part of Springer Nature 2021

## Abstract

We investigate both experimentally and using a computational model how the power of the electroencephalogram (EEG) recorded in human subjects tracks the presentation of sounds with acoustic intensities that increase exponentially (looming) or remain constant (flat). We focus on the link between this EEG tracking response, behavioral reaction times and the time scale of fluctuations in the resting state, which show considerable inter-subject variability. Looming sounds are shown to generally elicit a sustained power increase in the alpha and beta frequency bands. In contrast, flat sounds only elicit a transient upsurge at frequencies ranging from 7 to 45 Hz. Likewise, reaction times (RTs) in an audio-tactile task at different latencies from sound onset also present significant differences between sound types. RTs decrease with increasing looming intensities, i.e. as the sense of urgency increases, but remain constant with stationary flat intensities. We define the reaction time variation or “gain” during looming sound presentation, and show that higher RT gains are associated with stronger correlations between EEG power responses and sound intensity. Higher RT gain further entails higher relative power differences between loom and flat in the alpha and beta bands. The full-width-at-half-maximum of the autocorrelation function of the eyes-closed resting state EEG also increases with RT gain. The effects are topographically located over the central and frontal electrodes. A computational model reveals that the increase in stimulus–response correlation in subjects with slower resting state fluctuations is expected when EEG power fluctuations at each electrode and in a given band are viewed as simple coupled low-pass filtered noise processes jointly driven by the sound intensity. The model assumes that the strength of stimulus–power coupling is proportional to RT gain in different coupling scenarios, suggesting a mechanism by which slower resting state fluctuations enhance EEG response and shorten reaction times.

**Keywords** Looming and flat sound · EEG · Resting state · Inter-subject variability · Ornstein–Uhlenbeck process · Multisensory integration

---

Handling Editor: Benedetta Franceschiello.

---

A. Longtin and G. Northoff are joint senior authors.

---

This is one of several papers published together in Brain Topography on the “Special Issue: Computational Modeling and M/EEG”.

---

✉ B. Sancristóbal  
bdesancristobal@elisava.net

<sup>1</sup> Physics Department, University of Ottawa, 150 Louis Pasteur, Ottawa, ON K1N 6N5, Canada

<sup>2</sup> Royal’s Institute of Mental Health Research, University of Ottawa, 1145 Carling Avenue, Ottawa, ON K1Z 7K4, Canada

<sup>3</sup> Department of Neuroscience, Imaging and Clinical Science and Institute of Advanced Biomedical Technologies, University G. D’Annunzio, 66100 Chieti, Italy

## Introduction

The ability to track changes in our environment relies on sensory processing (Wark et al. 2007). In order to perform appropriate motor responses (Heekeren et al. 2008; Ploran


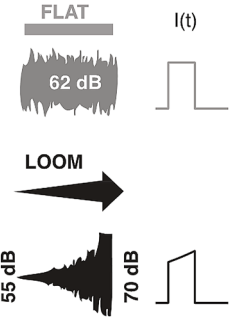

<sup>4</sup> Brain and Mind Research Institute, University of Ottawa, 451 Smyth Road, Ottawa, ON K1H 8M5, Canada

<sup>5</sup> Centre for Cognition and Brain Disorders, Normal University Hangzhou, Hangzhou 31121, China

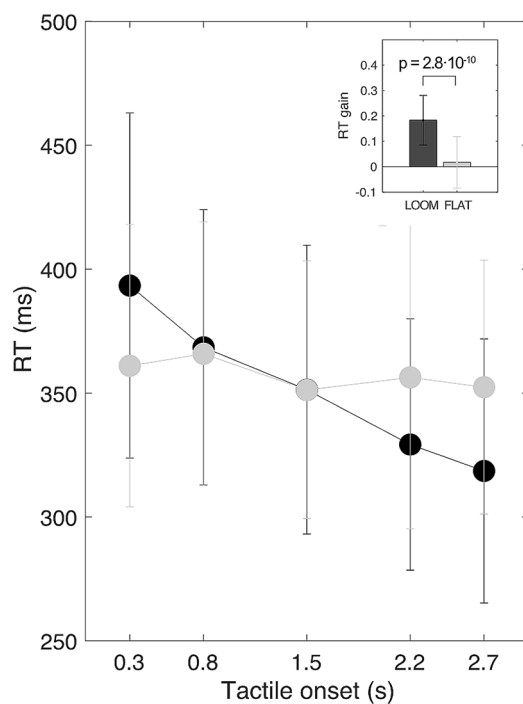
<sup>6</sup> Research Center for Mind, Brain, and Learning, National Chengchi University, Taipei City 11605, Taiwan

<sup>7</sup> Present Address: ELISAVA University School of Design and Engineering, Barcelona, Spain

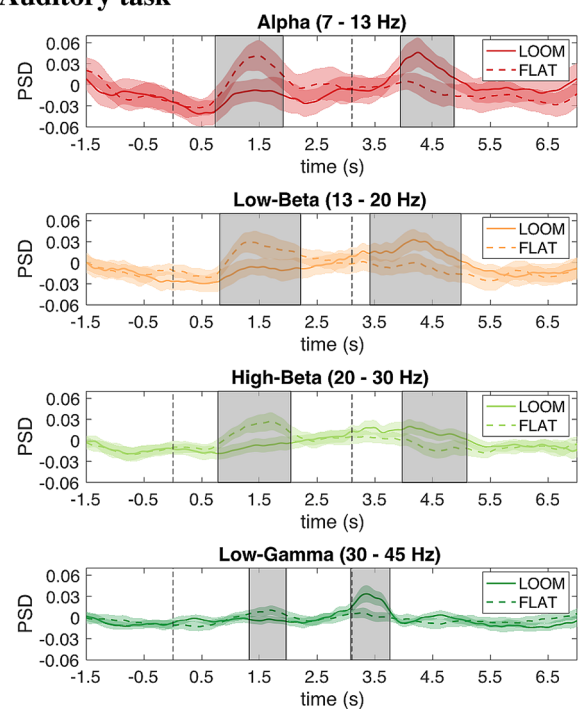
## a Experimental paradigm

	EEG	Auditory stimuli	Tactile stimuli	Measures
				
<b>Behavioral audio-tactile task</b>		X	X	Reaction Times (RT)
<b>Auditory task</b>	X	X		Stimulus-response correlation ( $\rho$ ) EEG power difference ( $PSD_{L-F}$ )
<b>Resting state session</b>	X			Autocorrelation window (ACW)

## b Behavioral audio-tactile task



## c Auditory task



**Fig. 1** Behavioral audio-tactile and auditory tasks. **a** Experimental paradigm showing the distribution of the three methodological features (EEG acquisition, auditory and tactile stimulation) and the measures used in the manuscript to quantify the data obtained in each session. FLAT and LOOM sounds correspond to the static (constant intensity) and dynamic (exponentially increasing intensity) sound presentation respectively (see Materials and Methods). The looming sound is felt as an object approaching the body (Ferri et al. 2015). **b** Behavioral audio-tactile task. Along with the auditory stimulation, in 60% of trials, participants were also presented with a tactile stimulus at one of five randomly chosen delays from sound onset. Trial-averaged reaction times (RTs) to the tactile target during looming sound (black circles) decrease at longer delays when the object feels closer. RTs during flat sound presentation (grey circles) remain approximately constant. The error bars represent one standard deviation around the mean, computed across all subjects. The inset shows the RT gain (see Materials and Methods) averaged across subjects for both sound conditions. **c** Auditory task. Trial-average dynamic course of power spectral density (PSD) for loom (solid lines) and flat (dashed lines) sounds computed in four different frequency bands after taking the mean across artifact-free channels and subjects (see Materials and Methods). The shaded areas correspond to the 95% confidence interval across the population. Sound delivery starts at time 0 (left vertical dashed line) and ends at 3.1 s (right vertical dashed line). The grey patches show the time windows where there is a significant difference between the two signals after temporal clustering (see Materials and Methods). Licenses for the EEG CAP and pointing hand are provided: *EEG Cap—The Noun Project icon from the Noun Project* by CIV is licensed under CC0 1.0 Universal. *Pointing hand cursor vector, mouse cursor, mouseover* by Manuel Campanoli is licensed under CC0 1.0 Universal

et al. 2007; Werkle-Bergner et al. 2014) we need to discriminate between threatening and innocuous signals (Dean et al. 2005). This implies that, at the neuronal level, sensory information needs to be dynamically transformed into movement preparation and action or, if appropriate, into a withholding of a reaction. In particular, cues that predict a possible collision of an object with our body are among the most salient stimuli coming from the environment. However, inter-individual differences in sensory perception due to distinct prior experiences, genetic background or neural diseases (Kanai and Rees 2011; Nielsen et al. 2008) modulate the ability of each subject to react. Even in simple experimental setups, where each sensory modality can be set apart from the rest and conditions are homogenous across participants, inter-individual response variability persists (Marder 2011).

In this study we have looked for signatures in the EEG that can explain variability across subjects to auditory responses to two types of sounds inducing different response patterns, both at the behavioral and electrophysiological level. In our experiment, subjects undergo three types of sessions that are performed sequentially as follows (Fig. 1a). First, they perform a behavioral audio-tactile task where a tactile stimulation prompts subjects to react at varying latencies from sound onset (Ferri et al. 2015). The acoustic intensity of the sounds used is either exponentially increasing (loom) or constant (flat). Second,

the EEG is recorded during two separate resting state sessions with eyes closed and in the absence of any stimulus to obtain the spontaneous brain dynamics of each subject that cannot be explained by attentional fluctuations during a task. Finally, an auditory task follows, where only loom and flat sounds were delivered and the EEG was also simultaneously recorded. Therefore, in the latest recording session there was no tactile stimulation, and thus no multimodal processing occurred and no reaction was required from the subject. This constitutes a No-report paradigm (Tsuchiya et al. 2015). The arrangement of the tasks allows us to investigate whether differences in the RTs between subjects (audio-tactile task) prevail (a) across their EEG power responses to sounds in the absence of any instruction to prepare a response (auditory task) and (b) across individual features of the spontaneous EEG power (resting state session).

Several studies have shown that the so-called spontaneous fluctuations affect stimulus-related responses. Pre-stimulus oscillatory power influences sensory perception, particularly in the alpha (Hanslmayr et al. 2007; Thut et al. 2006) and beta bands (Lange et al. 2012; Linkenkaer-Hansen et al. 2004). And the variability of responses across stimulus repetitions has been linked to fluctuations in either the amplitude and/or the phase of the ongoing activity (Arieli et al. 1996; He 2013; Huang et al. 2017; Linkenkaer-Hansen et al. 2001; Murray et al. 2014; Saka 2010; Saka et al. 2012), such that the recorded activity cannot be solely explained by the input. Moreover, slow scale-free fluctuations in resting state EEG activity and in reaction times series were comparable during a perceptual task (Palva et al. 2013), during timing-error sequences in a finger-tapping task (Smit et al. 2013) and during reaction-time (RT) performance (Irrmischer et al. 2018). Here, we present evidence that the temporal structure of the spontaneous activity, quantified by the full-width-at-half-maximum of its autocorrelation function (ACF)—also known as autocorrelation window (ACW)—, varies between subjects with different behavioral and electrophysiological responses to the sounds. Specifically, in the alpha and beta band, subjects with stronger RT modulation during the looming sound presentation show, on average, stronger stimulus–response correlation ( $\rho$ ) (i.e. acoustic intensity-EEG power correlation), and better neural differentiation of loom versus flat sounds. This group also exhibits longer ACWs.

Finally, we use a computational model to demonstrate how the effects of longer ACW could be related to  $\rho$  when viewing resting state fluctuations in EEG power as simple low-pass filtered noise. Noise is a significant component of brain activity across brain states (Xing et al. 2012), including in the alpha band of interest below (Lopes Da Silva et al. 1997; Lefebvre et al. 2017). Simple, low-dimensional non-linear dynamical system models of EEG have been proposed (Jansen and Rit 1995), as well as modular compositions of

such model into larger brain networks (David and Friston 2003) in which stochastic inputs play an essential role. While these and other modeling frameworks include external inputs, limited work has been devoted to understanding how the EEG tracks dynamical stimuli.

Here, we propose a model of brain dynamics constrained by the observation that the time scale of resting state fluctuations in a given band influences stimulus–response correlation in that band. This link has been generally overlooked, in part due to the natural tendency to express time in a model in units of such internal time scales. We show that simple linear stochastic models can be adapted to understand the evolution of EEG auditory responses to dynamic stimuli, and further provide insights into the dependence of these responses on resting state properties.

Our paper is organized as follows. We first compute the power spectral density (PSD) of the EEG signal in different frequency bands during looming and flat sounds, and the RTs as a function of the cue time after sound onset. The variation of the RT with the sound time course is quantified as an RT gain. Two groups of participants are defined according to a median split of the RT gain in the loom condition. This split is further justified from the performance of a machine learning-based classifier. This subdivision of the population is then used to examine the relationship between this gain and the neuronal responses during the auditory task, which are quantified by the difference in PSD during loom and flat sounds,  $PSD_{L-F}$ , and the stimulus–response correlation  $\rho$ . The relationship between RT gain and the resting state recordings is also examined using ACW. All measures reveal significant changes across the two groups in a frequency-dependent manner. The topographic distribution of such changes is then analyzed. Channels that display the strongest gap between groups reveal a clearer spatial segregation. Finally, we discuss a simple model where the power fluctuations are described as lowpass-filtered noise and show that its power–sound correlation is expected to increase with ACW, as in our data. A Discussion of our results follows, highlighting that many of these properties of EEG power with sound intensity follow from the simple assumption that these power fluctuations are adequately described as noise.

## Materials and Methods

### Experimental Design

#### Participants

Thirty-eight healthy volunteers (12 females, mean age 21.8 years, range 20–31) participated in the auditory and behavioral audio-tactile task, as well as in the resting state recording sessions. All the participants were right-handed

and provided written informed consent before participating in the study. The experimental protocol was approved by the University G. D’Annunzio of Chieti institutional ethics committee.

#### Auditory Stimuli

The auditory stimuli presented in both tasks (Fig. 1a) were samples of pink noise of 3100 ms duration with constant (flat) or increasing (looming) intensity levels. The sounds were sampled at 44.1 kHz. Sound intensity was manipulated using Soundforge4.5 software (Sonic Foundry) so that looming sounds had exponentially rising acoustic intensity from 55 to 70 dB of sound pressure level (SPL), whereas flat sounds remained at 62.5 dB SPL (Canzoneri et al. 2012; Ferri et al. 2015). During the auditory task, sounds were delivered by headphones (specifically designed for fMRI—see below—and connected to a NordicNeuroLab audio system), whereas during the behavioral audio-tactile task, two loudspeakers were used. It has been previously shown (Ferri et al. 2015) that perceived stimulus distance is not affected by these different experimental setups.

#### Tactile Stimuli

Tactile stimuli, presented during the behavioral sessions, were delivered using constant-current electrical stimulators (DS7A; Digitimer) via pairs of neurological electrodes placed on the hairy surface of the index fingers. The electrical stimulus was a single, constant voltage, rectangular monophasic pulse. At the beginning of each session, the intensity of the tactile stimulus was set to be clearly above threshold individually for each participant (Canzoneri et al. 2012). Intensity of the stimulator was set at the minimum value and then progressively increased until the participant reported to clearly perceive the stimulation. Next, the participant was presented with a sequence of 10 stimuli, intermingled with five catch trials in which no stimulation was presented. He/she was asked to report when he/she felt the tactile stimulus. If the participant did not perform 100% correctly (i.e., if he/she failed to respond to some stimuli or gave false positives to the catch trials), the intensity was further increased by a 5 mA step and the procedure was repeated. Intensity for the tested participants ranged between 60 and 90 mA. Stimulus duration was equal to 100  $\mu$ s.

#### EEG Acquisition

During a single session measurement, the EEG was recorded simultaneously with fMRI at 3 T Philips Achieva using MR compatible devices. A 64-channel BrainAmp MR system (Brain Products GmbH, Germany) was used for EEG recordings, along with the BrainCap electrode cap (Falk Minow

Services, Herrsching-Breitbrunn, Germany). All of the electrodes, which were placed on the scalp according to the international 10–10 system, were ring-type sintered non-magnetic Ag/AgCl electrodes. An additional channel was dedicated to the electrocardiogram (ECG) and to the EOG. The reference electrode was predefined in the cap and positioned in correspondence of the FCz electrode. The ground electrode was predefined and placed at Iz. The impedance of each electrode was maintained lower than 10 k $\Omega$  by means of electrode paste. The resolution and dynamic range of the EEG acquisition system were 100 nV and  $\pm 3.2$  mV, respectively. EEG data were acquired at 5 kHz using the Brain Vision Recorder v2.0 software (Brain Products GmbH, Germany) with a band-pass filter of 0.016–250 Hz. The Sync Box device (Brain Products, GmbH, Germany) was used to synchronize the hardware clock of the EEG with the MRI scanner's gradient switching system.

### EEG Data Pre-processing

The acquired EEG data were first pre-processed with a Brain Vision Analyzer (Brain Products, Munich, Germany). Gradient artifact correction was performed using the method proposed by (Allen et al. 2000) and incorporated into the Brain Vision Analyzer v.2.0. Data were down-sampled to 500 Hz using a Hanning-decimation process during the gradient correction and then exported in Matlab format for the following preprocessing step. Using a self-developed software implemented in Matlab (Mathworks, Sherborn, MA), the data were digitally filtered from 0.5 to 60 Hz using a Chebyshev II-type filter with 40 dB attenuation and zero-phase distortion, along with 50 Hz and 18.5 Hz notch filtering with a bandwidth of 1 Hz and 0.5 Hz respectively. The segments in all runs with high gross motion artifacts were rejected from further analysis using an automatic mode by setting a threshold of 100 microvolts for all subjects. A procedure based on independent component analysis (ICA) (Comon 1994; Hyvärinen and Oja 2000) was used for the rejection of ballistocardiographic artefact, ocular movements and the residual imaging artefact from the EEG data (Mantini et al. 2007; Vanderperren et al. 2010). The result was visually inspected to confirm the quality control. Before carrying out the following analyses, the EEG data were re-referenced to the average of all channels.

### Behavioral Audio-Tactile Task

On their first day, participants were blindfolded and comfortably seated beside a table with their right arm resting palm down. The audio-tactile apparatus, which was mounted on the table, consisted of two loudspeakers, one placed near to the participants' right hand and the other at a distance of 100 cm from the near loudspeaker (i.e., far from the

participant) and a constant-current electrical stimulator controlling a pair of neurological electrodes attached on the participant's right index finger. During each trial, either a looming or a flat sound was presented. Along with the auditory stimulation, in 60% of trials, participants were also presented with a tactile stimulus. The remaining trials (40% of total) were catch trials with auditory stimulation only (either looming or flat sounds).

The tactile stimulus was delivered at varying temporal delays from the onset of the auditory stimulus. Five different temporal delays were used:  $T_1 = 300$  ms;  $T_2 = 800$  ms;  $T_3 = 1500$  ms;  $T_4 = 2200$  ms; and  $T_5 = 2700$  ms. Each trial was followed by an inter-trial interval of 1000 ms. Each participant was presented with a random combination of 18 looming and 18 flat sounds for each temporal delay, randomly intermingled with the catch trials. Trials were equally divided into three blocks. Participants were asked to respond as fast as possible to the tactile target, when present, by pressing a button on a response box (Cedrus RB-834) with their left index finger, trying to ignore the auditory stimulus. The presentation of auditory and tactile stimuli, as well as the recording of participants' responses, were controlled by custom software implemented in MATLAB (The MathWorks). The RT gain was defined as  $\frac{RT(T_1) - RT(T_5)}{RT(T_1)}$ .

### Resting State Session

On the second day, each participant underwent two 5 min-runs of resting state (no stimuli). Following Honey et al. 2012 an analysis was performed on each individual channel to detect spectral bursts, which may indicate epileptiform activity or an intermittent electrode contact. A spectral burst was defined as a power value more than six times the interquartile range away from the median of the power time course in any frequency. Channels with at least one spectral burst (1109 from  $62 \times 38 = 2356$  total) in the resting state sessions were excluded here and in the following auditory task.

### Auditory Task

Following the resting state session, participants underwent two consecutive 6 min-runs of passive listening to looming and flat sounds equally distributed across the two runs. For the latter, a total of 30 auditory stimuli for each condition (looming and flat) occurred with an inter-stimulus interval (ISI) randomly selected between the values of 4.65, 6.2, or 7.75 s, and subjects were instructed to pay attention to the sounds. Participants were blindfolded and asked to keep their eyes closed. After artifact rejection was applied to the EEG data (see Sect. "EEG acquisition" below), the average

number of trials for the loom condition was  $25 \pm 3.4$  and for the flat,  $26 \pm 3.4$  (mean  $\pm$  std).

### Calculation of the Power Spectral Density and Selection of Frequency Bands

The time course of the power spectral density (PSD) was computed for each channel without spectral bursts for each participant. The PSD was estimated using the multi-taper method (Thomson 1982) commonly used to reduce the variance of the spectra of recorded signals, which are usually very noisy (Sancristóbal et al. 2013). This estimator was implemented in Chronux 2.10 (Bokil et al. 2010). The multi-tapered power spectrum,  $S(f)$ , is the average of the power spectrum of the EEG signal multiplied by  $K$  orthogonal Slepian functions:

$$S(f) = \frac{1}{K} \sum_{k=1}^K \left| \widehat{EEG}_k(f) \right|^2$$

where  $\widehat{EEG}_k(f)$  is the discrete Fourier transform of the EEG( $t$ ) signal multiplied by the  $k$ -th Slepian function (or taper). Following Honey et al 2012, we have used  $K=3$  tapers and  $S(f)$  was computed on data segments of 1 s every 10 ms, padded with zeros up to a length of 512 to obtain an increased sampling rate in the frequency domain. The bandwidth was set to 4 Hz.

For the recordings from the auditory task, we extracted trials for looming and flat sound presentation, starting at  $-1.50$  s and ending at  $7.0$  s from onset (note that the minimum distance between the onset of two subsequent  $3.10$  s long auditory stimuli is  $3.10$  s +  $4.65$  s =  $7.75$  s, corresponding to the smallest ISI of  $4.65$  s). Next, we applied a full-epoch length single-trial correction by dividing each trial by its temporal mean before trial-averaging. Then we defined the PSD by taking the logarithm after averaging across trials. Finally, the PSD within the alpha ( $7$ – $13$  Hz), low-beta ( $13$ – $20$  Hz), high-beta ( $20$ – $30$  Hz) and low-gamma ( $30$ – $45$  Hz) bands was obtained by averaging across the constituent frequencies.

### Pearson's Correlation Coefficient

The stimulus–response correlation  $\rho$  between the neuronal response  $x(t)$  and the intensity of the looming sound  $I(t)$  was computed as follows and implemented in Matlab through the `xcov` function:

$$\rho = \frac{\sum_{n=0}^{N-1} \left( x_n - \frac{1}{N} \sum_{i=0}^{N-1} x_i \right) \left( I_n - \frac{1}{N} \sum_{i=0}^{N-1} I_i \right)}{\sigma_x \sigma_I}$$

where  $x_n(t)$  are successive time samples of  $x(t)$ . The response  $x(t)$  is either the PSD obtained from the experimental EEG data defined in the previous section or the trial-averaged Ornstein–Uhlenbeck process defined in the Computational model section.  $\sigma$  is the unbiased standard deviation  $\frac{1}{N-1} \sum_{i=0}^{N-1} \left( x_i - \frac{1}{N} \sum_{i=0}^{N-1} x_i \right)^2$ .  $N$  is the number of scalar observations of each variable. We note that the time samples of the sound stimulus intensity  $I_n$  are the same for every trial, as it is not a stochastic process.

### Autocorrelation Window (ACW)

We used the definition in Honey et al. 2012, where ACW is computed as the full-width-at-half-maximum of the autocorrelation function (ACF) of the PSD in each frequency band. The time course of the resting state power in a given frequency band was normalized by its temporal average in that frequency band, and the logarithm was taken before defining the PSD in each band. Then, the time course is divided into  $20$  s blocks with  $10$  s overlap, and the ACF is computed in each block. The ACW is extracted from the averaged ACF over these blocks.  $\overline{ACW}$  is defined as the ACW averaged across the two resting state runs, and  $\langle \overline{ACW} \rangle_{\text{subjects}}$  is the  $\overline{ACW}$  averaged across subjects. Only one participant presented inconsistency between the ACW computed in the two runs and was removed from the analysis in Fig. 3 and other analyses as well.

### Statistical Analysis

#### Temporal Clustering

We compute the  $t$ -value at every time point as  $t = \frac{\bar{x}}{\sigma/\sqrt{n}}$ , where  $\bar{x}$  is the average across subjects of the variable  $x$  that is being tested against the null hypothesis,  $\sigma$  is the standard deviation between subjects and  $n$  the number of subjects.  $t$ -values decrease for high variance of the sample (high  $\sigma$ ), for small samples (low  $n$ ), and for low sample mean (low  $\bar{x}$ ). Hence, greater  $t$ -values provide greater evidence against the null hypothesis. In Fig. 1c,  $\bar{x}$  is the difference between power in the loom and the flat conditions, i.e.  $\text{PSD}_{L-F}$ , and the null hypothesis considers that there is no difference between the response to the two sounds.

Significance is set at  $p$ -values below  $0.05$ , which corresponds to a  $t$ -value =  $\pm 2.024$ , for  $n=38$ . Then we test whether the length of clusters of consecutive time points where  $|\bar{x}| \geq 2.024$  are larger than obtained by chance. To do so we built a permutation distribution of lengths of clusters under the null hypothesis that consists of shuffling the sound-label for each subject, thus creating  $10,000$  resamplings of the observed data. The proportion of permuted values that are larger than the observed ones sets the

significance for each temporal cluster of the data (Maris and Oostenveld 2007).

### Confidence Intervals

For approximately normally distributed variables (such as the log transformed power), the upper and lower bounds of the 95% confidence intervals are computed from the Student's  $t$  distribution evaluated at the probability 0.025 and 0.975.

### Classification Algorithm

We use a logistic regression algorithm (*mnrfit* MATLAB function) to classify whether a subject belongs to the high or low RT gain group defined by a median split of the RT gain in the loom condition. The logistic function that is implemented is defined as:

$$\log\left(\frac{p(\text{high})}{1-p(\text{high})}\right) = b_o + \sum_i b_i \cdot x_i$$

where the predictor variables are the  $x_i$ 's and correspond to  $\text{PSD}_{L-F}$  computed at the sound onset,  $\rho$  and  $\text{ACW}$  for low and high beta and averaged over the highlighted electrodes in Fig. 5 ( $3 \times 2$  features). The regression coefficients  $b_i$  index the direction and strength of the relationship between individual estimates of  $x_i$  and the probability of belonging to the high RT gain group.  $b_o$  is the model intercept or bias. We apply a tenfold cross validation. Hence, on every run of the classifier we obtain 10 values for the prediction accuracy (i.e. the percentage of correct classifications) evaluated in a different data set (randomly chosen 40% of the data) than the one used for the training set (the 60% left). In both the training and test set we ensure the same number of subjects in each group. In order to test whether prediction accuracy is significantly different than chance, we have run 10,000 times the described classifier, randomly assigning the high/low RT gain group to the true observations  $x_i$ . The true prediction accuracy is compared against the distribution of accuracies from the null-hypothesis to obtain a p-value.

### Computational Model

We have used the Euler–Maruyama algorithm to integrate the stochastic differential equation Eq. (2) in the Results, known as the Ornstein–Uhlenbeck process. The time step was set to  $10^{-4}$ . The autocorrelation time constant  $\tau$  and the variance  $\sigma^2$  are obtained from the resting state recording and are frequency and channel specific (Fig. 6d). The external current  $I(t)$  mimics the increase in acoustic intensity of the looming sound during the 3.1 s. The rate of increase is

linked to the time course of the intensity by  $\beta = \frac{1}{T} \ln\left(\frac{I_F}{I_o}\right)$ , where  $T = 3.1$  s is the duration of the sound,  $I_F = 70$  dB SPL and  $I_o = 55$  dB SPL for the looming sound, and for the flat sound  $I = 62.5$  dB SPL (see “Auditory Stimuli” section above). The coupling strength between  $I(t)$  and the stochastic process  $x(t)$  was assigned a different value for the low and high RT gain groups.

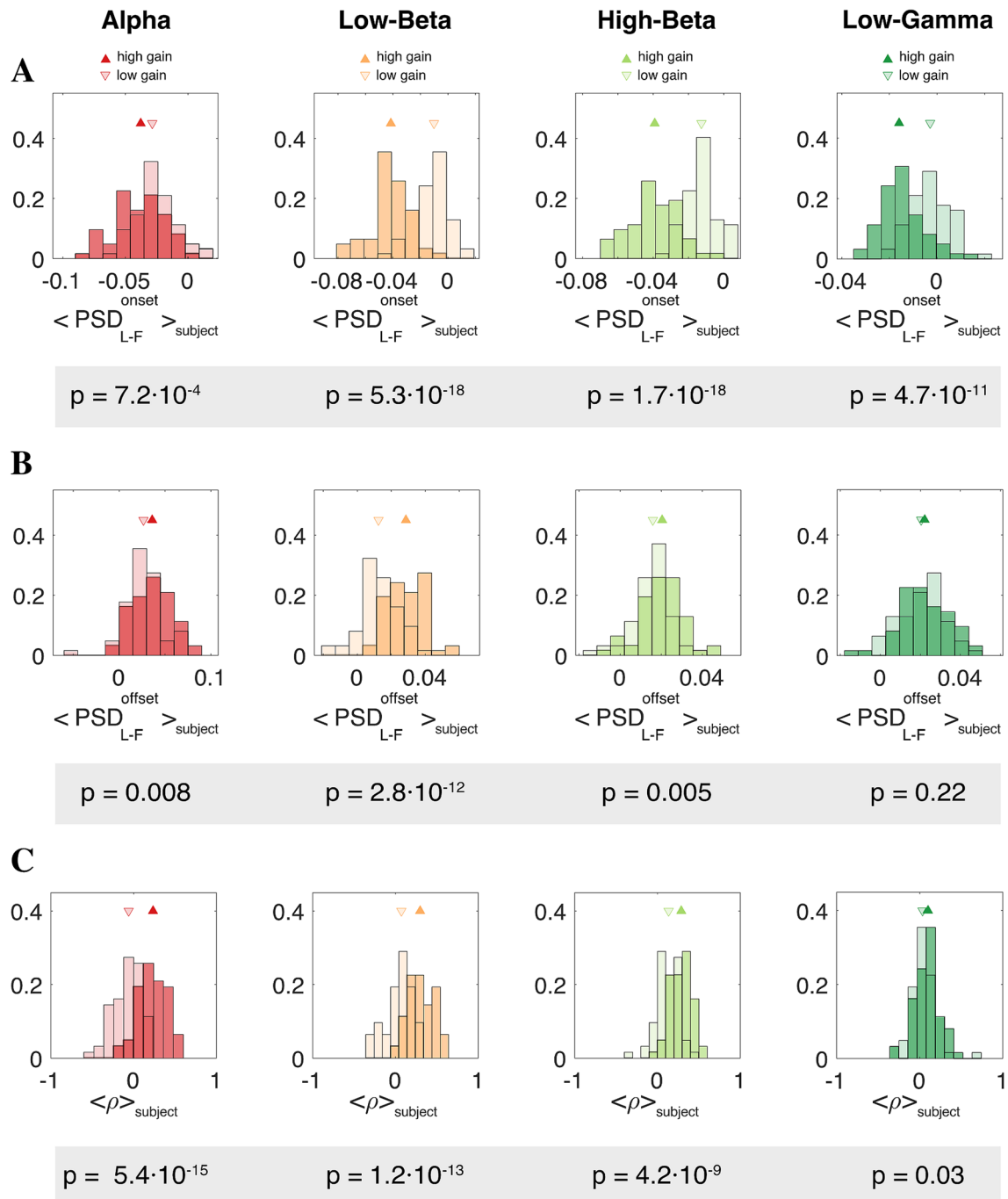
### Results

We first examined the reaction times to the tactile stimulus in the multimodal auditory-tactile task. The RTs were assessed following tactile cues,  $T_1$ – $T_5$ , delivered randomly at one of five times after the onset of loom and flat sound stimulus depicted in Fig. 1a (see “Materials and Methods”). Figure 1b shows RT as a function of the five onset times, averaged across trials and subjects. Under the flat sound intensity condition, little variation in the RT is observed. For the looming stimulus, however, there is a clear decreasing trend in which the RT shortens as the sound becomes louder. The RT gain, defined as  $\frac{\text{RT}(T_1) - \text{RT}(T_5)}{\text{RT}(T_1)}$ , averaged across subjects along with its standard deviation, is shown in the inset. The RT gain is clearly much larger in the looming condition, such that a louder sound speeds up the tactile task (sign test,  $p = 2.8 \cdot 10^{-10}$ ).

The neural response to the looming and flat sounds is measured by the PSD of the EEG signal recorded during the auditory task and filtered into the various bands of interest (see “Materials and Methods”). The PSD revealed distinctive patterns between conditions in the alpha (7–13 Hz), low-beta (13–20 Hz), high-beta (20–30 Hz), and low-gamma (30–45 Hz) bands (Fig. 1c). After sound onset, at about  $\sim 0.7$  s later, power responses of either sound start to separate significantly with respect to baseline.

The onset response is more marked for the flat sound, which turns on with an intensity that is halfway between the minimum and maximum intensities used in the looming condition (Fig. 1a). This onset increase in power is followed by a decrease around 1.5 s after flat stimulus onset, after which power reverts to baseline before the offset of the stimulus (Maier and Ghazanfar 2007). In contrast, the EEG power tracks the intensity of the looming sound, although an onset response is clearly seen and displays a peak at about the same time as the one seen for the flat sound. Within a second or so of this first peak, the power resumes its increase with the looming sound; this is the case in the three lower frequency bands of interest here. We also notice in the looming case an offset response that peaks between 0.5 and 1.0 s after the stimulus ends, thereby leaving a remnant in the post-stimulus period. These results are in agreement with

## Behavioral audio-tactile task – Auditory task



**Fig. 2** Effect of RT gain on the auditory task. Histograms across channels of the PSD during loom minus the PSD during flat sound presentation,  $\text{PSD}_{L-F}$ , computed within the significant window **a** after sound onset and **b** after sound offset (see grey boxes in Fig. 1c). **c** Histogram across channels of the stimulus–response correlation,  $\rho$ , between the EEG power and the acoustic intensity of the looming sound. Quantities are averages across subjects,  $\langle \dots \rangle_{\text{subject}}$ , within

two groups according to whether their RT gain in the loom condition (black bar in Fig. 1b inset) is above its median (dark colors/upward triangles) or below (light colors/downward triangles). Tables in gray show the p-value of a one-sided Wilcoxon rank sum test where the alternative hypothesis is that the high RT gain histogram has a median lower (**a**), or greater (**b**, **c**) than the low RT gain histogram



the psychophysical finding that ramped sounds are heard as being longer than steady sounds (Grassi and Darwin 2006). Grey boxes are displayed in each frequency band, which bracket the times during which the EEG power during loom minus the EEG power during flat sound presentation,  $\langle \text{PSD}_{L-F} \rangle_{\text{subject}}$ , is significantly different than zero.

Panels in Fig. 2 show the distribution across channels of  $\langle \text{PSD}_{L-F} \rangle_{\text{subject}}$  after averaging across participants with high RT gain (dark colors/upward triangles) and low RT gain (light colors/downward triangles) computed within the significant window (A) towards sound onset and (B) towards sound offset (see grey boxes in Fig. 1c). These groups are determined through a median split of the RT gain distribution computed in the loom condition. The median of the distributions is marked with a triangle. In all bands, the high RT gain group shows  $\langle \text{PSD}_{L-F}^{\text{onset}} \rangle_{\text{subject}}$  values around sound onset that are more negative than in the low RT gain group, while  $\langle \text{PSD}_{L-F}^{\text{offset}} \rangle_{\text{subject}}$  are more positive. Therefore, the  $\text{PSD}_{L-F}$  statistic takes on more extreme values in the high RT gain group.

Of particular interest is the correlation of the EEG power fluctuations with the stimulus intensity. We next show results for the Pearson linear correlation  $\rho$ , or stimulus–response correlation for brevity, between the looming sound intensity and its corresponding EEG power response in the different bands in Fig. 2c. Correlations tend to be more positive in the high RT gain group than in the low RT gain group particularly in the alpha and beta bands. Gray tables in Fig. 2a–c summarize all the p-values for testing the null hypothesis of no difference between the medians of the two distributions.

These results indicate that a high RT gain corresponds to more sensitivity to the type of sound being played not only reflected in a subject's behavior but also in its neuronal activity across the scalp. By performing a median split on the data, we do not suggest that there are two inherent groups of participants (indeed, the distribution of RT gain is unimodal). This analysis rather shows that channel-based EEG related variables of the auditory task significantly change between groups that, by construction, have different mean RT gains, even in the absence of a linear correlation between these variables. We will later support an RT split using a machine learning-based classifier.

Next, we test our hypothesis that higher behavioral and neuronal responsiveness in subjects can be explained by differences in the dynamics of their spontaneous brain activity, which we quantify by the time scale of the EEG power fluctuations during rest or autocorrelation window (ACW). ACW measures the width of the resting state autocorrelation function around its origin (i.e. around zero lag). The left panel of Fig. 3a shows two superposed ACFs, one for the activity in the alpha band (red), and the other for the activity in the high-beta band (green) for a particular subject and

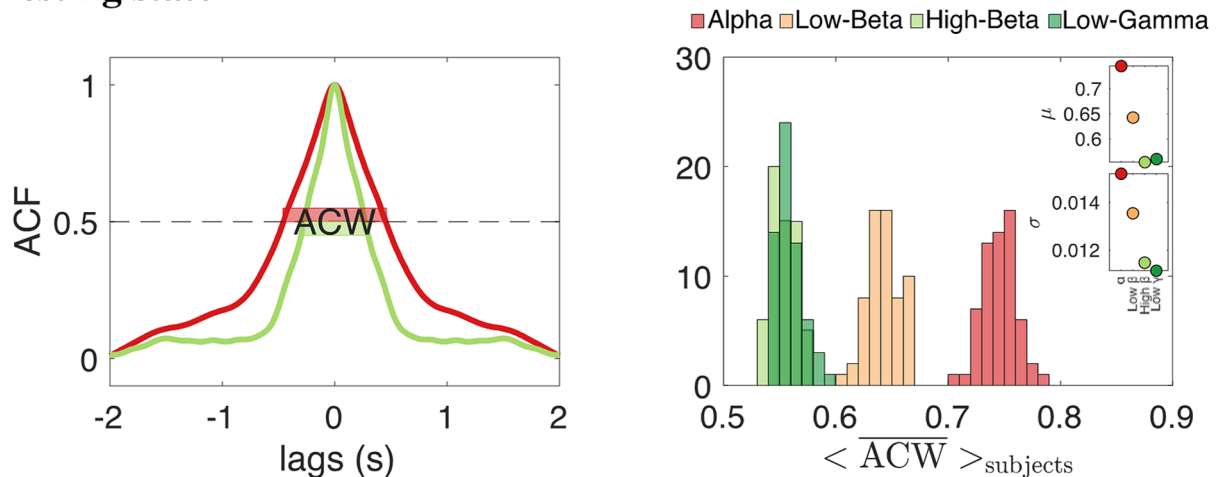
electrode located in the occipital lobe. It is clear from this panel that the ACW for the alpha band is larger than that for the high-beta band, implying that the power fluctuations in the alpha band occur on a slightly slower time scale than those in the high-beta band. This tendency is in fact preserved when averaging across subjects and pooling all channels, as the right panel of Fig. 3a shows. The  $\langle \text{ACW} \rangle_{\text{subject}}$  values in alpha stand out from those computed in the other bands. We also observe that the mean of the  $\langle \text{ACW} \rangle_{\text{subject}}$  distribution increases as the frequency content of the band decreases (top inset). Figure 3a further reveals that the distributions of  $\langle \text{ACW} \rangle_{\text{subject}}$  values are narrower as the frequency of the band increases (bottom inset).

Figure 3b shows that in the alpha and beta bands, higher RT gain participants exhibit longer ACW, since the distribution of ACW averaged across participants within this group is higher than the corresponding distribution of the low RT gain group. A link between the auditory task and the resting state session can also be established by comparing  $\langle \text{PSD}_{L-F} \rangle_{\text{subject}}$  and  $\langle \rho \rangle_{\text{subject}}$  with  $\langle \text{ACW} \rangle_{\text{subject}}$ . In Fig. 4, each of the variables measured in the auditory task is plotted against  $\langle \text{ACW} \rangle_{\text{subject}}$ , where the average is taken separately for the high and low RT gain participants. Hence, for each channel, population averages within the low RT gain group (light colors) and for the high RT gain group (dark colors) are simultaneously shown on each axis. Means for the low and high RT groups are shown with downward and upward triangles, respectively. Below each panel, the correlation coefficient  $r$  quantifies the linear relationship between the y and x coordinates, as well as the corresponding p-value. Most of the statistically significant  $r$  values occur in the alpha and low-beta bands. We have seen that auditory evoked changes in EEG are heterogeneous across the scalp and are larger for the high RT participants (Fig. 2). Now, Fig. 4 reveals that such variability is consistent with a similar variation of ACW. We will later examine with a computational model whether these relationships can be causal.

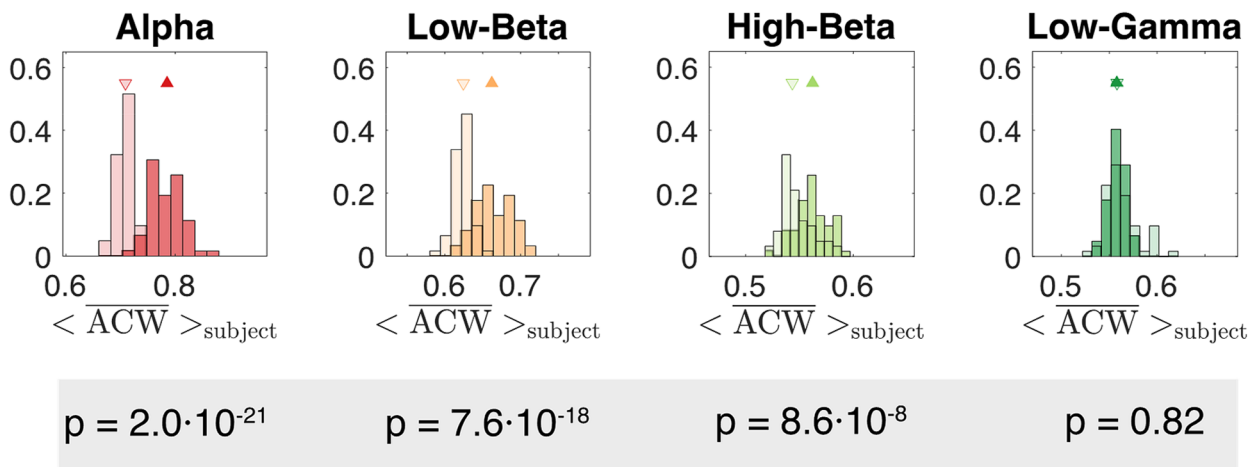
So far, the connection between the behavioral audio-tactile task and the different EEG recording sessions has been studied by pooling all channels separately for the high and low RT gain groups (Figs. 2, 3, 4). It is possible, though, that not all brain areas are involved in the explicit and implicit demands of each task, and that the PSD time course of only some of the electrodes shows more pronounced differences between participants in the measures characterizing the auditory task ( $\rho$  and  $\text{PSD}_{L-F}$ ) and the resting state (ACW).

Thus, we next explore which channels contribute more to the horizontal separation of the upward and downward triangles in all panels of Figs. 2, 3b, which denote averages within the high RT gain group and within the low RT gain group, respectively. To do so, we have plotted the spatial distribution of such differences between high and low RT groups,  $\Delta \langle \dots \rangle_{\text{subject}}$ . In order to account for the varying

## A Resting state



## B Behavioral audio-tactile task – Resting state



**Fig. 3** Effect of RT gain on the autocorrelation window during rest. **(a left)** Two autocorrelation functions (ACF) of the PSD computed from the EEG during a resting state session (see “Materials and Methods”) for electrode O1. The red line corresponds to the ACF computed from the EEG power fluctuations in the alpha band. The light green line is the corresponding ACF of the signal in the high-beta band. The horizontal colored bars at the half-maximum (horizontal dashed line,  $ACF=0.5$ ) define the length of the autocorrelation window (ACW) for each ACF. **(a right)** Distribution of the ACW

across channels, averaged over the two resting state runs,  $\overline{ACW}$ , and over subjects,  $\langle \overline{ACW} \rangle_{\text{subjects}}$ , for the different frequency bands. The insets display the mean (top) and standard deviation (bottom) of the distributions. **b** Histograms across channels of  $\langle \overline{ACW} \rangle_{\text{subjects}}$  for the participants with high RT gain (dark colors/upward triangles) and low RT gain (light colors/downward triangles). The gray table shows the p-value of a one-sided Wilcoxon rank sum test where the alternative hypothesis is that a high RT gain histogram has higher median than the low RT gain histogram

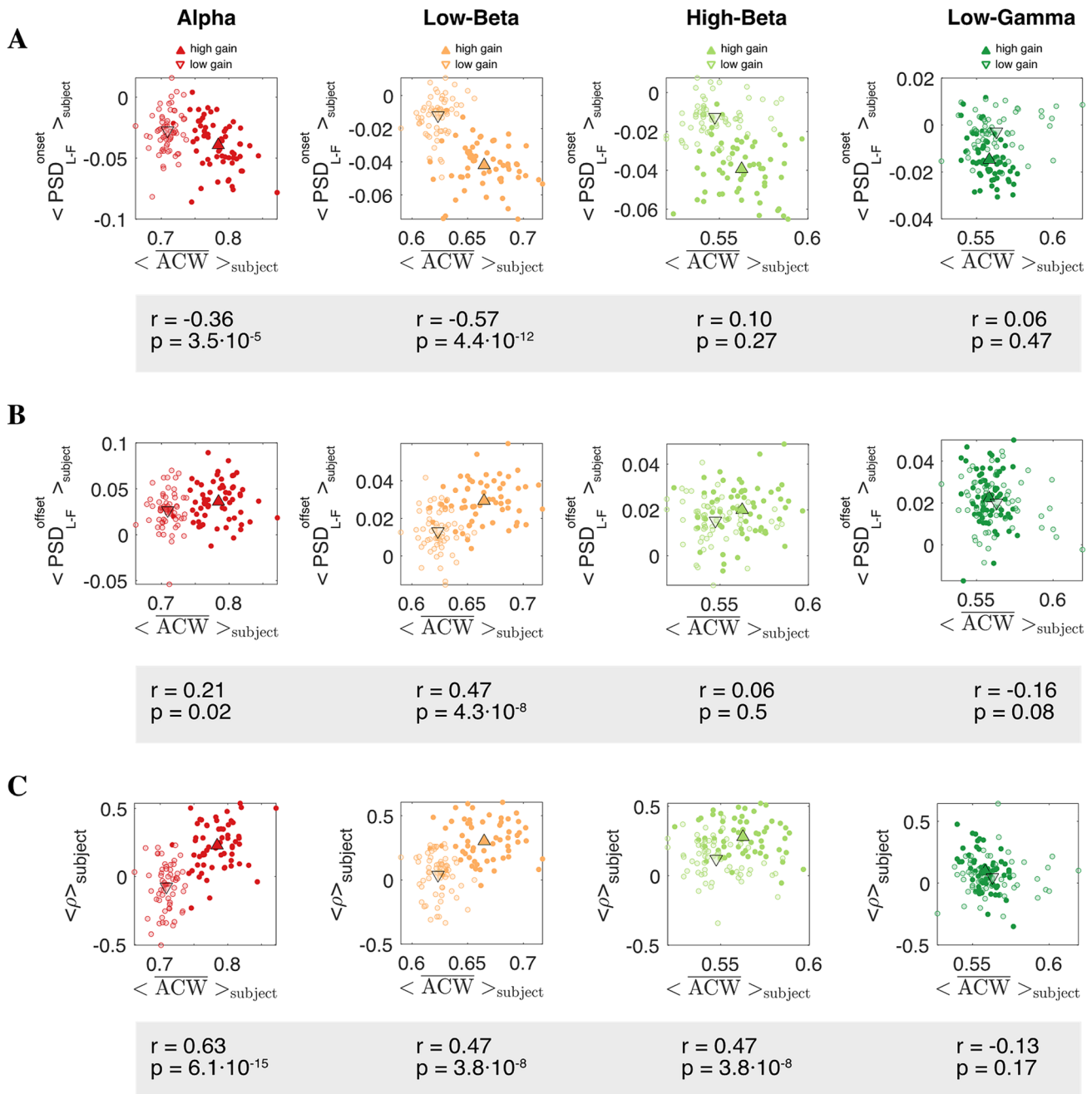
width of the histograms across frequency bands and computed variables, we show the standard score (or z-score). Channels that lead to a z-score  $\geq 1.5$  ( $\leq -1.5$  for  $PSD_{L-F}^{\text{onset}}$ ) are highlighted and labeled (Fig. 5) and correspond to the locations where  $PSD_{L-F}$ ,  $\rho$  and  $\overline{ACW}$  better correlate with the RT gain (see Supplementary Figures S1 and S2 for an example of a highlighted and non-highlighted channel, respectively).

We quantify the similarity of the topographic maps in each band by computing the correlation matrix between all

four variables (bottom matrices in Fig. 5). For each comparison, we show in the upper triangular portion of the matrix the scatter plots between the x and y coordinates labeled in the horizontal and vertical axis, respectively. The corresponding correlation coefficients R and p-values are shown in the lower triangular portion of the matrix, symmetric to the diagonal.

In all four bands,  $\Delta \langle PSD_{L-F}^{\text{onset}} \rangle_{\text{subject}}$  and  $\Delta \langle PSD_{L-F}^{\text{offset}} \rangle_{\text{subject}}$  are anti-correlated (compare blue vs warm colors on similar

## Behavioral audio-tactile task – Auditory task – Resting state

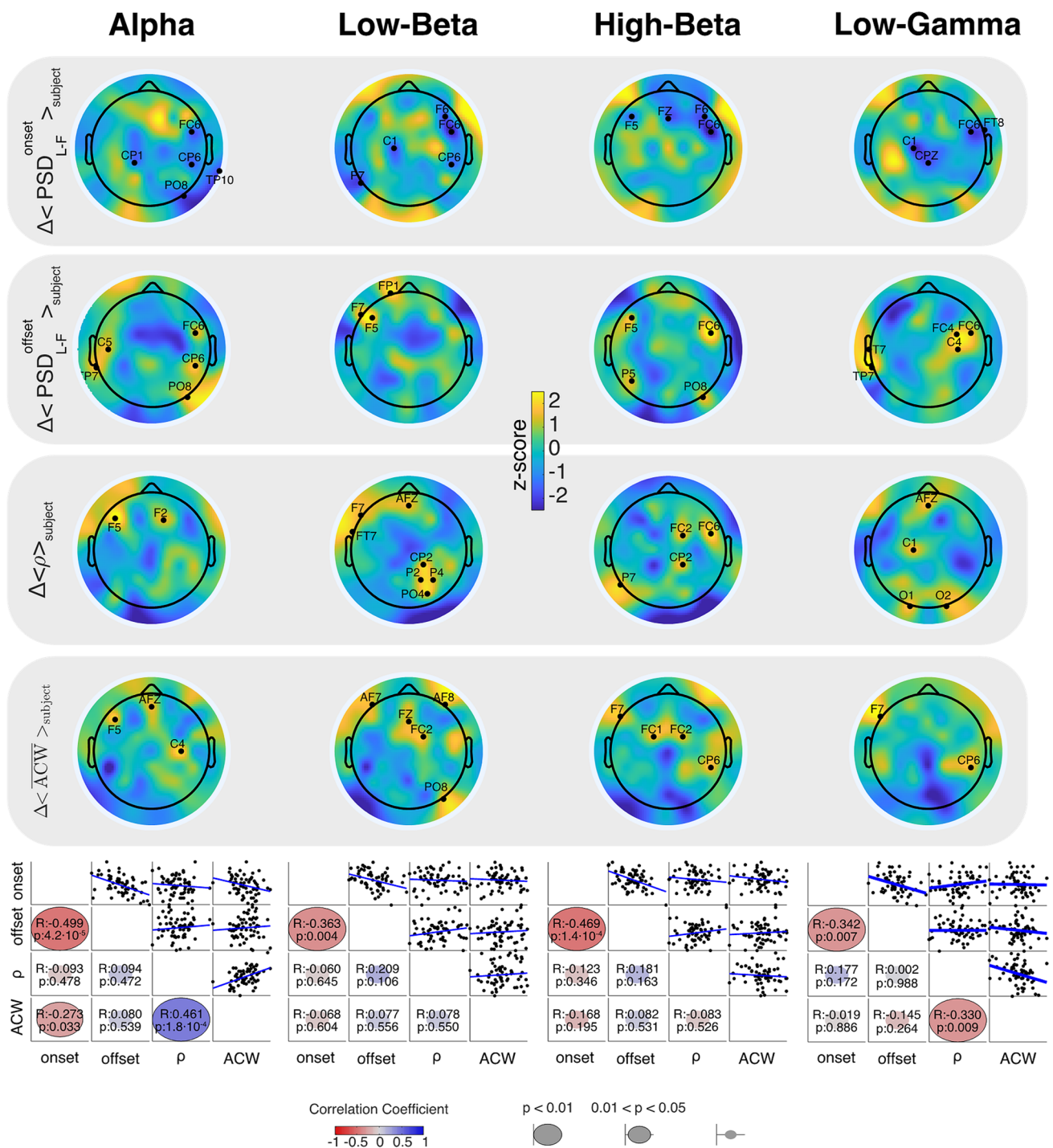


**Fig. 4** Effect of ACW on the auditory task. The variation  $\text{PSD}_{L-F}$  in PSD responses to loom and flat sounds is computed for each electrode and averaged within the two RT gain groups separately. This is done in the significant window after stimulus onset in **a** and after stimulus offset in **b** and plotted against the corresponding  $\langle \overline{ACW} \rangle_{\text{subjects}}$ . For each electrode, panel **c** shows  $\langle \rho \rangle_{\text{subjects}}$  within the

electrodes), meaning that similar areas are involved in the stronger power amplitude responses to flat and loom sounds of the high RT gain participants. However, none of these areas are involved in changes in  $\rho$  or ACW, which are found

two RT gain groups and plotted against  $\langle \overline{ACW} \rangle_{\text{subjects}}$ . A gray table below panels **a–c** shows the Pearson cross-correlation coefficient  $r$  between the variables shown in the y-axis in the panel above and  $\langle \overline{ACW} \rangle_{\text{subjects}}$  (x-axis), along with its p value. Upward (downward) triangles show the average across the high (low) RT gain group

to be significant in other areas. Interestingly,  $\Delta \langle \rho \rangle_{\text{subject}}$  and  $\Delta \langle \overline{ACW} \rangle_{\text{subject}}$  are maximally correlated in alpha, where they share similar topographies. Specifically, relevant electrodes



**Fig. 5** Topographic distribution of the differences  $\Delta$  between the high and low RT gain groups. Each of the quantities computed from the EEG power during the auditory task ( $\text{PSD}_{L-F}^{\text{onset}}$ ,  $\text{PSD}_{L-F}^{\text{offset}}$  and  $\rho$ ) and during the resting state (ACW) have been averaged across the participants within each RT gain group separately. The spatial distribution across the scalp of the standard score (z-score) of each of these differences ( $\text{PSD}_{L-F}^{\text{onset}}$ ,  $\text{PSD}_{L-F}^{\text{offset}}$ ,  $\Delta\rho$  and ACW) is shown in each frequency band. Black circles indicate the location of the electrodes

where  $z\text{-score} \geq 1.5$  ( $\leq -1.5$  for  $\text{PSD}_{L-F}^{\text{onset}}$ ). On the bottom, the correlation between these quantities in the four spatial maps for each band is shown (Lin 2015). On the upper triangular portion of the matrix, the scatterplots of the data in the x and y axis are shown. On the lower triangular portion of the matrix, we show the corresponding correlation values, R, and associated p-values. Correlation values and significance levels are also visualized as the color and sizes of circles, respectively

are located in the right centro-parietal regions and frontal areas.

Given the spatial heterogeneity of the effect of the median split on the variables obtained from the EEG power, we have only used data from the channels where the EEG power features show the highest difference between RT gain groups (shown in Fig. 5 as black circles) to train a multinomial logistic regression to classify whether a subject belongs to the high or low RT gain group. Each subject is determined by a selection of features, namely its  $\text{PSD}_{L-F}^{\text{onset}}$ ,  $\rho$  and  $\overline{\text{ACW}}$  computed in the beta band, where the number of relevant channels is the highest (see Material and Methods). Due to the collinearity between  $\Delta\langle\text{PSD}_{L-F}^{\text{onset}}\rangle_{\text{subject}}$  and  $\Delta\langle\text{PSD}_{L-F}^{\text{offset}}\rangle_{\text{subject}}$  (shown by the correlation matrices in Fig. 5), we have only used the former as a predictor. The accuracy of such a classifier,  $0.63 \pm 0.13$ , is significantly higher than chance ( $p = 0.04$ ).

### Computational Model of Auto-correlation Window and Sensory-Related Activity

Our analysis shows that individuals with significantly different temporal scales of EEG power fluctuations during rest, quantified by the  $\overline{\text{ACW}}$ , respond with different neuronal patterns to both the looming and flat sound. Yet it is not clear whether there is anything beyond this correlation in terms of causation, and if so, what possible mechanism could underlie causation. A precise answer is currently not within reach given our data. But a beginning of an answer can be obtained by considering a simple computational model that is calibrated on the resting state to reproduce basic features of the spontaneous dynamics of the EEG power, and then driven by the acoustic stimulus.

We demonstrate that, by only assuming that the EEG power fluctuations are a manifestation of linearly filtered noise, we can qualitatively reproduce the results shown in Fig. 4c, namely, the stimulus–response correlations across the brain are higher for the high RT gain group, and their changes are linearly correlated with changes in  $\overline{\text{ACW}}$ . This was done without assuming any detail about brain structure, circuitry, rhythm dynamics, and neurochemistry. Our approach is in line with recent modeling work based on linear stochastic neural mass models with nonlinear delayed feedback to understand how brain states, i.e. spatiotemporal patterns of EEG and MEG, can be altered by external stimulation (Hutt et al. 2016; Lefebvre et al. 2017). We simplify their coupling between neural subsystems, as we seek the minimal ingredients required to reproduce the correlation between  $\overline{\text{ACW}}$  and  $\rho$  while accounting for RT gain.

Specifically, we assume that the EEG power fluctuations at each electrode in a given frequency band are governed by simple stochastic linear dynamics endowed with a finite correlation time,  $\tau$ . Therefore, the fluctuating EEG power at the

$i$ -th electrode is modeled as a random variable  $x_i(t)$  which has a tendency to revert to an equilibrium value, but is moved away from it by noise. Without loss of generality, we consider  $x(t)$  to be the zero-mean lowpass-filtered Gaussian white noise process, more precisely known as the Ornstein–Uhlenbeck (OU) noise process (Uhlenbeck and Ornstein 1930). Here we will adopt the scaling in Lindner and Longtin 2006, for which the power fluctuations  $x(t)$  in any given band and channel evolves according to the linear stochastic differential equation:

$$\frac{dx}{dt} = -\frac{1}{\tau}x(t) + \sqrt{\frac{2\sigma^2}{\tau}}\xi(t) \quad (1)$$

where  $\tau$  is the characteristic timescale of the exponential decay of the autocorrelation function  $\langle x(t)x(t+l) \rangle = \sigma^2 e^{-|l|/\tau}$  and  $\sigma$  is the strength of the Gaussian white noise process  $\xi(t)$  and determines the standard deviation of  $x(t)$ .

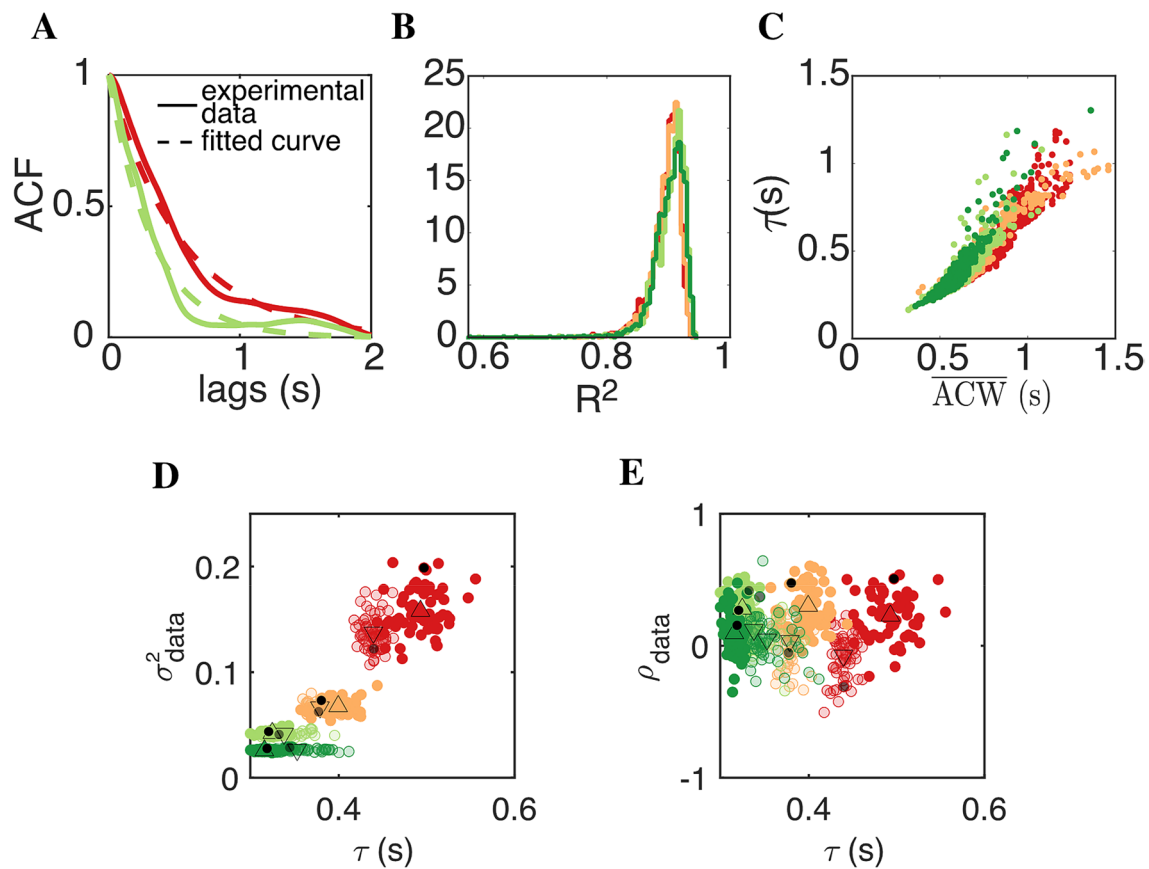
In order to extract the parameter  $\tau$  from the data, we compute the ACF for all positive lags for the same subject, channel and bands. Like in Figs. 3a, 6a shows two ACFs as solid colored lines and a fit of these data to a single exponential, as the OU process would have, with dashed colored lines. The distribution of the set of coefficients of determination,  $R^2$ , obtained from the fitting in each frequency band is left-skewed, meaning that some experimental ACF diverge from the exponential decay assumption (Fig. 6b). However, given that these distributions are quite narrow and show a clear peak around 0.9, the premise that power fluctuations are given by an OU process is reasonable. The parameter  $\tau$  obtained from the fitting is plotted against the experimental  $\overline{\text{ACW}}$  in Fig. 6c, showing that both quantities are directly proportional.

Finally, we also extract the variance from the resting state power signal to feed into our multivariate OU model. It is seen in Fig. 6d that the variance increases as the frequency of the band decreases. This is foremost a consequence of the fact that the power spectrum of the EEG in the lower frequency bands is higher. In our modeling below, we will constrain the variance of  $x(t)$  using these data.

As in the EEG recordings, we simulate as many OU processes as channels ( $N = 62$ ), each one with its own  $\tau_i$  and variance constrained by the data in Fig. 6d. We add to Eq. (1) two extra terms: one that accounts for the coupling between OU processes and another one that accounts for the external time-varying input current  $I(t)$  representing the sound, as in the auditory task:

$$\frac{dx_i}{dt} = -\frac{1}{\tau_i}x_i(t) + \sqrt{\frac{2\sigma_i^2}{\tau_i}}\xi_i(t) - A \frac{\sum_{j=1}^N (x_j(t) - x_i(t))}{\tau_i} + \frac{R_i}{\tau_i}I(t) \quad (2)$$

Our model is a simplified version of that used in (Hutt et al. 2016) in which the recurrent connectivity is simply



**Fig. 6** Lowpass-filtered noise model for resting state dynamics of EEG power fluctuations. **a** Fitting of an exponentially decaying autocorrelation function  $C(l, l) = \sigma^2 e^{-|l|/\tau}$  with  $\sigma=1$  (dashed line) over the experimental ACF (solid line) shown in Fig. 3a for all positive lags (red: alpha, green: high-beta). **b** Distributions of the coefficient of determination,  $R^2$ , of the fitting as in **a** in each color-coded frequency band and across channels. **c** The parameter  $\tau$  from the best fits in **b** versus the experimental ACW for each electrode shows a quasi-linear relationship in each frequency band. In each band, there are as many points as there are electrodes and subjects. **d** The vari-

ance of the resting state,  $\sigma^2$ , is plotted against the parameter  $\tau$  for each frequency band and channel separately.  $\sigma^2$  is averaged across the participants within the low (light colors) and high (dark colors) RT gain group separately. The black (high RT gain) and gray (low RT gain) circles mark the data that have been used in Fig. 7. **e** The stimulus–response correlation,  $\rho$ , is plotted against the parameter  $\tau$  for each frequency band and channel separately. Black/Gray circles are as in **d**. Color code as in previous figures. Upward (downward) triangles in **d** and **e** show the average across the high (low) RT gain group

a constant all-to-all diffusive coupling without delay and strength  $A$ . Note that the coupling term effectively decreases the variance of  $x_i(t)$ . In order to set the variance of  $x_i(t)$  equal to  $\sigma_{i,data}^2$  (Fig. 6d) we thus further needed to scale up  $\sigma_i^2$  in Eq. (2). We will simulate Eq. (2) when  $A=0$ , and all the OU processes are independent, and when  $A=0.1$ , in order to investigate whether the coupling influences the stimulus–response correlation and its dependence on electrode-specific ACW measures in the resting state.

The stimulus  $I(t)$ , added here to the standard OU process, increases exponentially as  $I_0 e^{\beta t}$  for the looming sound (Fig. 1a) (see “Materials and Methods”). Regarding the ratio of parameters  $\frac{R_i}{\tau_i}$ , we will examine two scenarios. First, we will assume that  $x_i(t)$  is a simple leaky integrator with an injected stimulus current, whose leak resistance  $R_i$  and time

constant  $\tau_i$  are proportional  $\frac{R_i}{\tau_i} = C$  and, thus,  $I(t)$  is not scaled by  $\tau_i$  (no scaling case). This yields the following dynamics:

$$\frac{dx_i}{dt} = -\frac{1}{\tau_i} x_i(t) + \sqrt{\frac{2\sigma_i^2}{\tau_i}} \xi_i(t) - A \frac{\sum_{j=1}^N (x_i(t) - x_j(t))}{\tau_i} + R' \cdot I(t)$$

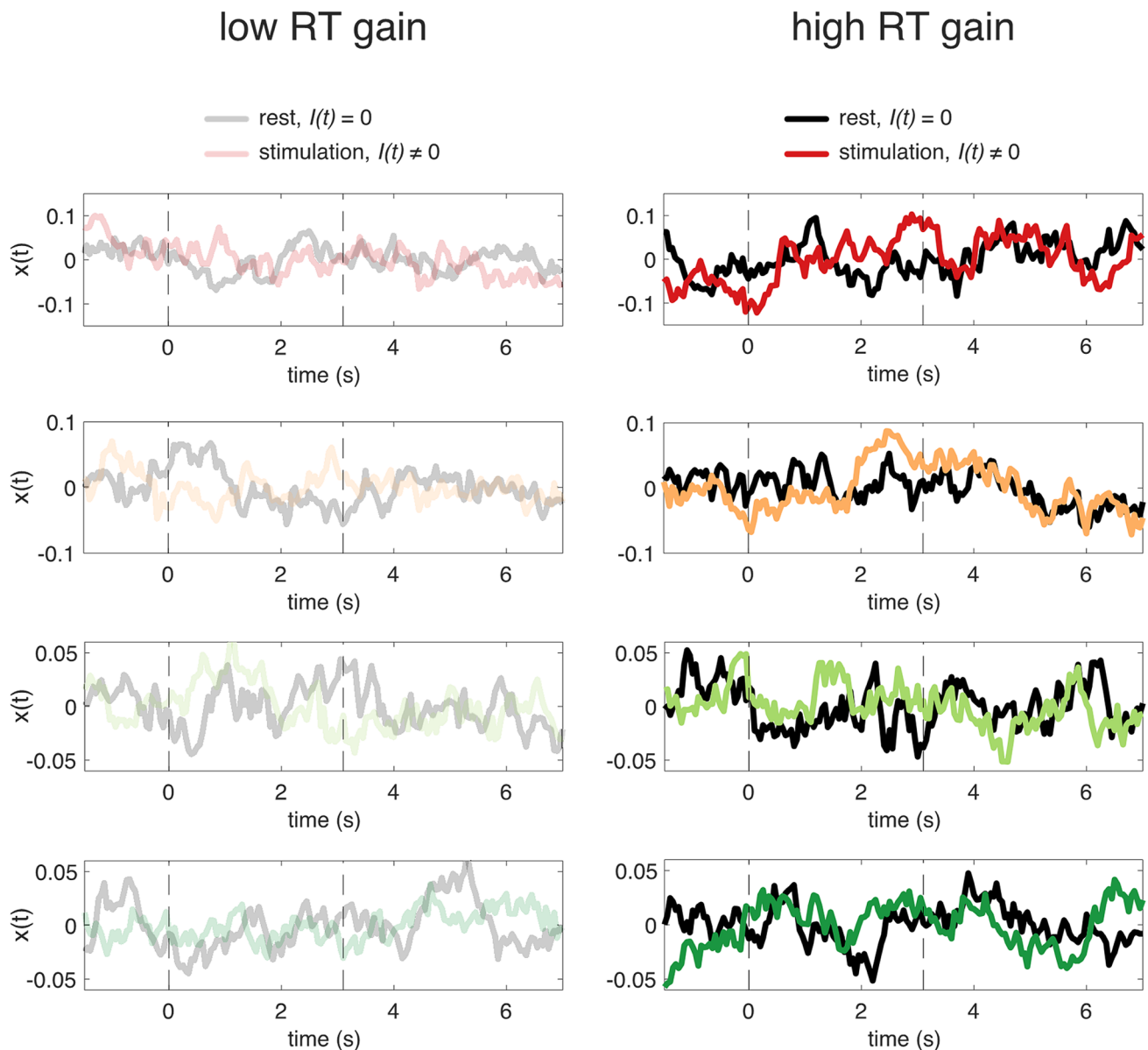
where  $R' = \frac{1}{C}$ .

Secondly, we will study the case where an EEG channel does not behave like a simple capacitor in parallel with a linear resistor, but is rather more complex and, thus,  $\frac{R_i}{\tau_i}$  is not constant and the  $I(t)$  is also divided by the system response time (scaling case). This now yields the following dynamics:

$$\frac{dx_i}{dt} = -\frac{1}{\tau_i}x_i(t) + \sqrt{\frac{2\sigma_i^2}{\tau_i}}\xi_i(t) - A\frac{\sum_{j=1}^N(x_i(t) - x_j(t))}{\tau_i} + \frac{R}{\tau_i}I(t)$$

With  $\tau_i$  and  $\sigma_i^2$  estimated from the resting state data, we aim at reproducing Fig. 4c, which is also shown in Fig. 6e by pooling all frequency bands in a single plot. Each dot represents data from one electrode, averaged across subjects

within the high (dark colors) and low (light colors) RT gain groups and after the EEG power has been averaged across presentations of the loom sound. The experimental results for individual bands appear in a staggered manner, i.e. moving from left to right as the frequency of the band decreases or, equivalently, as  $\tau$  increases. We observe a wide range of values of the correlation coefficient, with some negative ones but mainly positive ones. Moreover, a clear tendency



**Fig. 7** Realizations of the Ornstein-Uhlenbeck process as a band-specific model of power fluctuations (red: alpha, orange: low-beta, light green: high-beta, dark green: low-gamma). Time traces of a single channel from the integration of Eq. (2) in the uncoupled case ( $A=0$ ), and no scaling (i.e.  $\frac{R_i}{\tau_i} = C$ ). The left column corresponds to low values of the parameter  $R$  and the right column to high values of  $R$  that

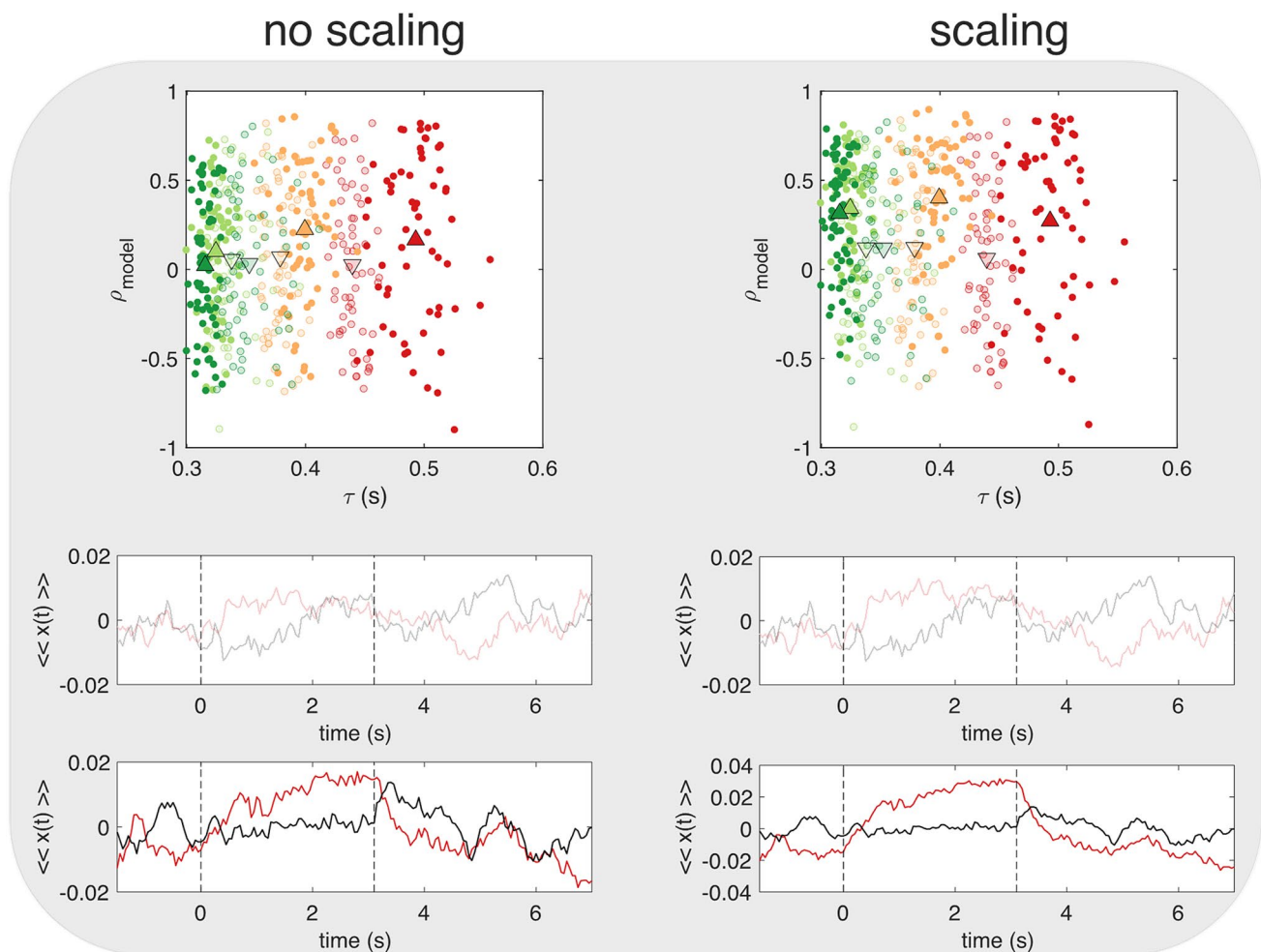
represent, respectively, low and high RT gains. Gray/black time traces correspond to the resting state simulations, where no input is present as in Eq. (1). Colored time traces correspond to the trial-average of  $x(t)$  after 100 presentations of the stimulus  $I(t) = I_0 e^{\beta t}$ . Vertical dashed lines delimit stimulus duration (as in Fig. 1c). In each panel of the left/right column,  $\tau$  and  $\sigma$  are assigned values based on our experimental data highlighted with thin/thick black circles in Fig. 6d

is visible, where high RT gain is associated with higher values of  $\rho$ . This cannot be solely explained by  $\tau$ , since higher changes in  $\rho$  occur between RT gain groups with smaller differences in  $\tau$  (compare, for instance, red upward and downward triangles for the mean of each RT gain group) than with larger  $\tau$  shifts (compare, for instance, red upward and orange downward triangles). We mimic this RT gain dependency by choosing two different  $R'$  (no scaling) or  $R$  (scaling): a weak one  $R'/R = 1.67 \cdot 10^{-4}$  for low RT gain subjects, and a higher one  $R'/R = 6.67 \cdot 10^{-4}$  for high RT gain subjects.

Time traces of  $x(t)$  for a single channel in the uncoupled and no scaling case for  $\tau$  and  $\sigma$  selected from Fig. 6d (black circles) for each different frequency band are shown in

Fig. 7 for the two  $R$  values (low value in the left column and high value in the right column). It can be also verified that, in agreement with Fig. 6e, the dark red (alpha band) and orange (low-beta band)  $x(t)$  time traces (high RT: right column Fig. 7) increase along with the sound (vertical dashed lines) as compared to the light red and orange  $x(t)$  (low RT: left column Fig. 7).

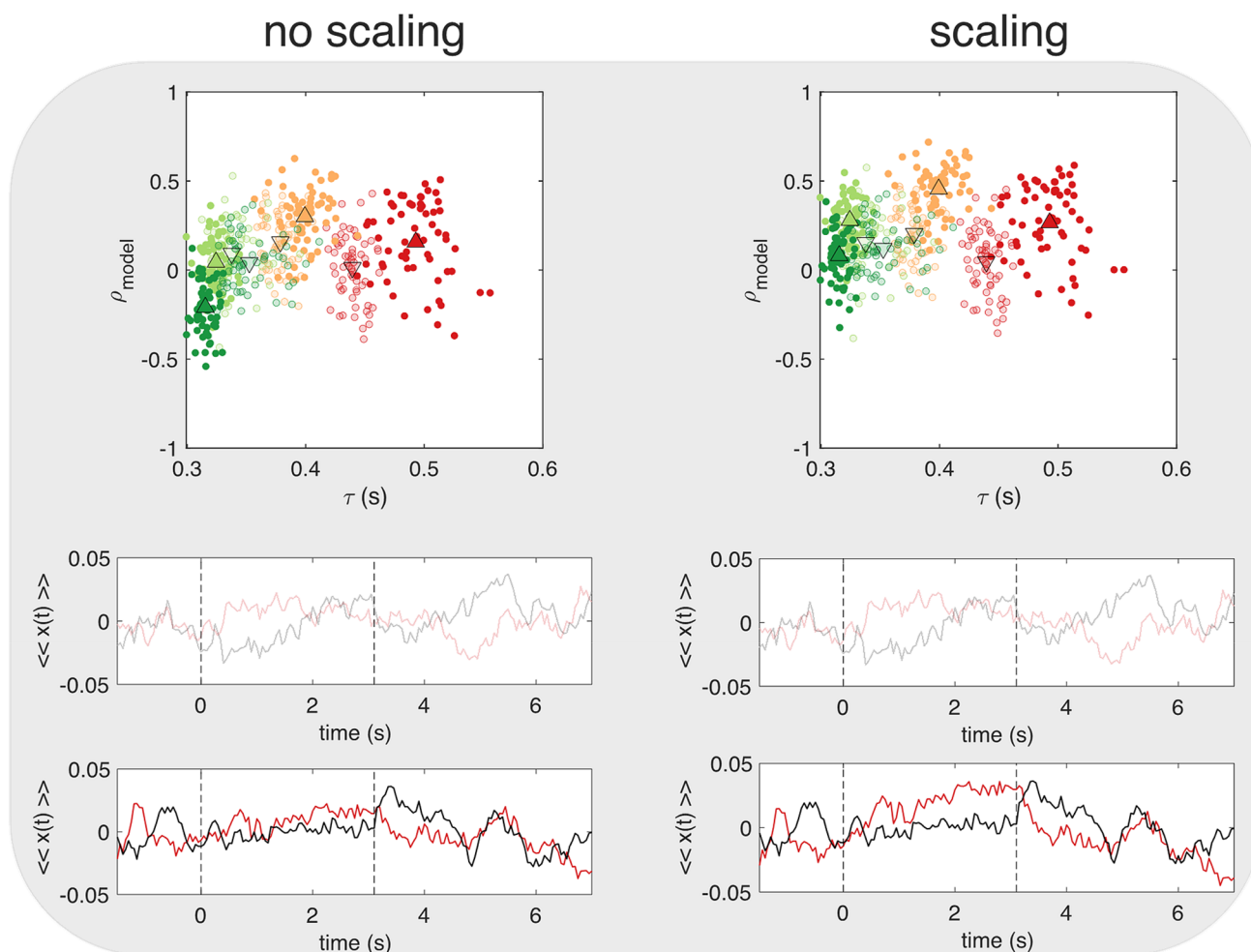
Figures 8 and 9 show the  $\rho$  versus  $\tau$  plot (to compare with Fig. 6e) when  $\rho$  is computed from the trial-averaged simulated electrode ensemble  $x(t)$  and  $\tau$  and the variance are constrained by the experimental data in Fig. 6d. Figure 8 represents the uncoupled electrode case and Fig. 9 the coupled case. Both show the results for the two scaling



**Fig. 8** Stimulus–response correlation for the uncoupled OU processes. Equation (2) is integrated when  $A=0$ , that is when the OU processes are uncoupled, and for the no scaling (left panels) and scaling (right panels) scenario. In the upper square panels, we plot the simulated correlation coefficients  $\rho$  against the parameter  $\tau$  obtained from the data. Each of the 62 OU processes in our model represents the activity in a channel whose variance and correlation time are calibrated using our experimental data for each channel (Fig. 6d).  $\rho$  is the stimulus–response correlation between the averaged response

of the OU process,  $x(t)$ , to  $N=100$  presentations of an exponentially increasing input stimulus  $I(t) = I_0 e^{\beta t}$  of 3.1 s of duration. Below each square plot, we show the trial and channel averaged responses corresponding to the experimental values of  $\tau$  within the alpha band (red dots in the square panels) and for the two RT gain groups, represented by different values of  $R$  in Eq. (2). Light colors correspond to low  $R$  and dark colors to high  $R$ . The resting state,  $I(t) = 0$ , is shown in black/gray





**Fig. 9** Stimulus–response correlation for the coupled OU processes. Equation (2) is integrated with  $A \neq 0$ , that is, when the OU processes representing the activities in each channel are coupled. This is done again for the no scaling (left panels) and scaling (right panels) scenario. The calibration of each electrode using the data in Fig. 6d leads to different noise strengths for each channel compared to Fig. 8 due to the effect of the coupling. In the upper square panels, we plot the simulated correlations  $\rho$  against the parameter  $\tau$  obtained from the data.  $\rho$  is again the stimulus–response correlation between the aver-

aged response of the OU process,  $x(t)$ , to  $N=100$  presentations of an exponentially increasing input stimulus  $I(t) = I_0 e^{\beta t}$  of 3.1 s duration. Below each square plot we show the trial and channel averaged responses corresponding to the experimental values of  $\tau$  within the alpha band (red dots in the square panels) and for the two RT gain groups, represented by different values of  $R$  in Eq. (2). Light colors correspond to low  $R$  and dark colors to high  $R$ . The resting state,  $I(t) = 0$ , is shown in black/gray

choices, although similar results are obtained. Greater effects occur when going from  $A = 0$  to  $A \neq 0$ , since the all-to-all coupling of the OU processes synchronizes the signals and the distribution of  $\rho$  shrinks and better resembles the data (Fig. 6e). Going from the no scaling to the scaling scenario effectively boosts the impact of  $I(t)$  by dividing it by  $\tau_i < 1$ .

This computational model thus shows that the effect of the correlation time of the OU processes, which is simply proportional to ACW, on the stimulus–response correlation can be replicated under simple assumptions of stimulus-driven low-pass filtered noise processes operating at each electrode and calibrated to mimic resting state activity

autocorrelation and variance. Slower resting state fluctuations (longer  $\tau$  values) can thus plausibly lead to better stimulus–response correlation. The simulation data further mimic the strong variability in the stimulus–response correlation across channels. The model reveals that a weak coupling amongst the channels can improve this correlation, especially under a stronger coupling to the stimulus in the high RT gain case. The higher RT gain can thus be seen as a higher signal-to-noise ratio for the stimulus-driven OU dynamics, which somehow reflects the overall responsiveness of the brain area and the impact of this responsiveness on multimodal processing.

## Discussion

Our study investigates how sensory-related activity is modulated by both the dynamics of acoustic stimuli and the spontaneous activity. The sounds used in this study differ in their temporal evolution and, as a consequence, in their implicit content: the looming sound is perceived as an approaching object whereas the flat is not. Therefore, the first provides changing information about the environment in relation to the body and the latter does not supply additional evidence apart from its onset and offset. In a previous study, a comparison between the perceived positions of these sounds in space revealed a significant reduction of the noticed distance from body with increasing intensity that was absent during flat sound presentations (Canzoneri et al. 2012; Ferri et al. 2015). Hence, even in the absence of a motor task, the passive perception of approaching, non-stationary sounds elicited an altered representation of the external space, probably due to an implicit urge to prepare a defensive action. Our ‘no-report’ paradigm (Tsuchiya et al. 2015) decouples perception from immediate action and allows to distinguish stimulus-related from task-related effects.

Human response times were found to vary along the looming sound in an audio-tactile multisensory task that demands a motor response cued by a tactile stimulus. The subject’s RT drops significantly as the sound intensity increases but remains relatively constant during the flat sound (Fig. 1b). The RT gain quantifies the strength of this drop, and is correlated with changes in certain EEG power statistics. A machine learning-based classifier that considers changes in particular channels and frequency bands of stimulus-EEG response correlation, ACW, and EEG power differences between the two auditory stimulus conditions, provides the justification for a median split of our subjects into low and high RT gain groups, even though there is clearly a continuum of such gain values. The low-vs-high RT gain split enabled us to succinctly summarize the trends in our data.

Further, these behavioral differences for loom versus flat sounds were accompanied by differences in alpha, beta, and low-gamma bands activity during an auditory uni-sensory task. EEG power following a flat sound onset relaxes back to baseline before the offset, while it builds up following a looming sound well into the post-stimulus period (Fig. 1c). These PSD patterns were quantified by differences in power during loom and flat,  $PSD_{L-F}$ , and by stimulus–response cross-correlation  $\rho$ . Similar results were reported in a study where the blood oxygen level-dependent (BOLD) signal in humans was greater for rising (looming) compared to constant (flat) intensity sounds across time (Seifritz et al. 2002). Comparable patterns of brain activity were also found in monkeys, where a sustained increase in gamma-band power

of the local field potential (LFP) signals in the auditory cortex was obtained during looming but not receding sound presentation (Maier and Ghazanfar 2007).

Our RT result are also compatible with a recent report of an auditory bias towards identifying more quickly a looming versus a receding stimulus (Bidelman and Myers 2020). That finding was based on an EEG source analysis in the 1–30 Hz range and establishes the involvement of the prefrontal cortex—and its functional connectivity to the primary auditory cortex—for processing such evolutionary important stimuli. Our study exposes the relevant dynamical features of the EEG during the looming phase, notably in the alpha and low-beta bands and their correlation with response speed. These features may reflect an influence from the PFC and underlie its involvement visible in Fig. 5 for stimulus–correlation in the lower frequency range.

PSD responses averaged across subjects with high RT gain are larger than those averaged across subjects with low RT gain (Fig. 2a, b). This is also true when comparing the loom stimulus–response correlation between the two groups (Fig. 2c) and the resting state temporal structure, as measured by ACW (Fig. 3b). Inter-individual variability during behavioral and perceptual tasks has been explained by variations in brain anatomy (Kanai and Rees 2011; Mueller et al. 2013) and EEG task-evoked activity (Drew and Vogel 2008; Martens et al. 2006). Our results suggest that this heterogeneity can also be explained by the temporal scale of spontaneous power fluctuations.

We found that, particularly in the alpha and beta bands, single-electrode measures of power amplitude during sound delivery and stimulus–response correlation with looming acoustic intensity changed across RT gain groups proportionally to changes in ACW (Fig. 4). Interestingly, only a subset of channels contributed to enhance such differences  $\Delta$  across participants with different RT gains (Fig. 5). For instance, the spatial distribution of electrodes with higher  $\Delta PSD_{L-F}$  was similar when computed both after sound onset and offset. This means that similar brain areas account for high changes in acoustic intensity in flat (onset) and loom (offset) sounds. Also, in alpha and beta, right centro-parietal and left frontal electrodes more specifically contributed to larger  $\Delta\rho$  and  $\Delta ACW$ .

Higher  $\rho$  values in the alpha band, as a proxy for the rise of PSD during looming sound, usually occur in those brain regions involved in movement planning, such as motor areas (Klimesch et al. 2007). Similar power accumulation in beta can potentially be attributed to previously reported increases in prefrontal beta power during inhibition of the motor system to suppress saccades in monkeys (Hwang et al. 2014). In humans, beta power increases in fronto-central areas during motor inhibition or in prefrontal regions during enhanced cognitive control when subjects had to cancel or change motor behavior (Liebrand et al. 2018). Although RTs and

EEG during sound presentation were not collected simultaneously, the stronger co-variation found between them in beta is consistent with studies examining volitional motor control. In monkeys, spontaneous increases in beta power or induced with neuro-feedback biased behavior towards slower movement onset (Khanna and Carmena 2017). Therefore, the increase in beta power during the loom condition in the auditory task can potentially reflect strong suppression of movement implicit in the perception of approaching stimuli. If this is so, a subject with a high  $\rho$  would be strongly pushing the brake over motor responses during the auditory task and would release it when an action is prompted during the audio-tactile task, which translates into a high RT gain. By examining subjects' time scale of the EEG power fluctuations during rest (ACW, Fig. 3) we were also able to determine that such a subject within the high RT gain group is intrinsically more reactive to sensory stimuli due to his/her longer ACW.

Finally, our computation model for resting state brain activity allows us to attribute a potential causal role for the magnitude of ACW on the neuronal and behavioral responses to sounds. There are two assumptions that underpin our modeling approach of power fluctuations as lowpass filtered Gaussian white noise (OU process). The first is simplicity: this noise has two parameters, namely its amplitude and its correlation time (or inverse bandwidth). It is thus the simplest level of complexity in modelling dynamical noise processes beyond the standard Gaussian white noise approach. It also acknowledges the fact that an OU process entails a stochastic signal that asymptotically reverts to its mean with a finite time scale. As the ACF shows (Fig. 3a), the experimental PSD corresponds to this type of damped dynamics whereby low values of ACW lead to fast relaxation to the mean. Indeed, the ACF of power fluctuations is well-fitted by an exponential, which is the property of an OU process. The second assumption is one of coupling simplicity between electrodes and to the external stimulus. This simplified, coarse-grained view of brain activity then leads to the conclusion that longer ACW may be causally linked to a stronger linear correlation between the sound stimulus and the EEG response.

Our modeling approach identifies minimal dynamical elements to account for observed stimulus–response correlations, as well as their dependence on resting state properties and their link to behavioral RTs in this multisensory scenario. Further experimental and computational work is needed to explain the nature of the stimulus–EEG and inter-electrode coupling strengths and their relation to the gain of the behavioral responses. Our assumption of linearly correlated noise is compatible with autoregressive models of EEG that represent activity fluctuations as a time-invariant

near-equilibrium linear thermal process (Wright et al. 1990). Future work could add local resonances and delayed interactions between areas (David and Friston 2003; Hutt et al. 2016; Jansen and Rit 1995; Nunez 2000) to seek improved agreement with our data in different bands. The effect of the stimulus on the response time could also be considered in a conductance-based formulation of our model. Adaptation which is visible in our power responses to flat stimuli, could also be considered as in (Lefebvre et al. 2017). These additions will deepen our understanding of the stimulus–resting state interactions in terms of time scale-specific interactions (Murray et al. 2014) beyond the ACW-dependent stimulus–response correlation described in our study.

## Conclusions

Our work provides evidence for the role of the resting state dynamics in modulating sensory-related and motor responses. The autocorrelation time constant, ACW, of resting state dynamics characterizes the temporal scale of ongoing EEG power and constrains its ability to track a looming versus a flat sound since it measures the scale at which perturbations away from average power decay. ACW can be considered a source of inter-individual variability in sound perception and behavior as supported by heterogeneous power responses and reaction times elicited by looming and flat sounds. In particular, participants with short ACW also exhibit a low modulation of their power dynamics and RT with sound intensity. Although the experimental data do not allow us to conclude a causal relationship between resting and active sensory states, our computational model allows us to conjecture that more responsive brains (neurally and behaviorally) are an endogenous property of slower spontaneous dynamics.

**Supplementary Information** The online version contains supplementary material available at <https://doi.org/10.1007/s10548-021-00826-4>.

**Acknowledgements** The authors would like to thank Gustavo Deco for his comments on an earlier version of the manuscript.

**Funding** This work was supported by the EJLB-Michael Smith Foundation (200809EJL-194083-EJL-CECA-179644), the Canada Institute of Health Research (CIHR, 201103MOP-244752-BSB-CECA-179644), and the Canada Research Chair (CRC) (to GN). AL was supported by NSERC Canada (RGPIN-2014-06204) and the University of Ottawa Research Chair in Neurophysics. The funders had no role in study design, data collection and analysis, decision to publish, or preparation of the manuscript.

**Declaration**

**Conflict of interest** The authors declare that they have no conflict of interest.

## References

- Allen PJ, Josephs O, Turner R (2000) A method for removing imaging artifact from continuous EEG recorded during functional MRI. *Neuroimage*. <https://doi.org/10.1006/nimg.2000.0599>
- Arieli A, Sterkin A, Grinvald A, Aertsen A (1996) Dynamics of ongoing activity: Explanation of the large variability in evoked cortical responses. *Science*. <https://doi.org/10.1126/science.273.5283.1868>
- Bidelman GM, Myers MH (2020) Frontal cortex selectively overrides auditory processing to bias perception for looming sonic motion. *Brain Res*. <https://doi.org/10.1016/j.brainres.2019.146507>
- Bokil H, Andrews P, Kulkarni JE, Mehta S, Mitra PP (2010) Chronux: a platform for analyzing neural signals. *J Neurosci Methods*. <https://doi.org/10.1016/j.jneumeth.2010.06.020>
- Canzoneri E, Magosso E, Serino A (2012) Dynamic sounds capture the boundaries of peripersonal space representation in humans. *PLoS ONE*. <https://doi.org/10.1371/journal.pone.0044306>
- Comon P (1994) Independent component analysis, a new concept? *Signal Process*. [https://doi.org/10.1016/0165-1684\(94\)90029-9](https://doi.org/10.1016/0165-1684(94)90029-9)
- David O, Friston KJ (2003) A neural mass model for MEG/EEG: coupling and neuronal dynamics. *Neuroimage*. <https://doi.org/10.1016/j.neuroimage.2003.07.015>
- Dean I, Harper NS, McAlpine D (2005) Neural population coding of sound level adapts to stimulus statistics. *Nat Neurosci*. <https://doi.org/10.1038/nn1541>
- Drew T, Vogel EK (2008) Neural measures of individual differences in selecting and tracking multiple moving objects. *J Neurosci*. <https://doi.org/10.1523/JNEUROSCI.0556-08.2008>
- Ferri F, Costantini M, Huang Z, Perrucci MG, Ferretti A, Romani GL, Northoff G (2015) Intertrial variability in the premotor cortex accounts for individual differences in peripersonal space. *J Neurosci*. <https://doi.org/10.1523/JNEUROSCI.1696-15.2015>
- Grassi M, Darwin CJ (2006) The subjective duration of ramped and damped sounds. *Percept Psychophys*. <https://doi.org/10.3758/BF03193737>
- Hanslmayr S, Aslan A, Staudigl T, Klimesch W, Herrmann CS, Bäuml KH (2007) Prestimulus oscillations predict visual perception performance between and within subjects. *Neuroimage*. <https://doi.org/10.1016/j.neuroimage.2007.07.011>
- He BJ (2013) Spontaneous and task-evoked brain activity negatively interact. *J Neurosci*. <https://doi.org/10.1523/JNEUROSCI.2922-12.2013>
- Heekeren HR, Marrett S, Ungerleider LG (2008) The neural systems that mediate human perceptual decision making. *Nat Rev Neurosci*. <https://doi.org/10.1038/nrn2374>
- Honey CJ, Thesen T, Donner TH, Silbert LJ, Carlson CE, Devinsky O, Doyle WK, Rubin N, Heeger DJ, Hasson U (2012) Slow cortical dynamics and the accumulation of information over long timescales. *Neuron*. <https://doi.org/10.1016/j.neuron.2012.08.011>
- Huang Z, Zhang J, Longtin A, Dumont G, Duncan NW, Pokorny J, Qin P, Dai R, Ferri F, Weng X, Northoff G (2017) Is there a non-additive interaction between spontaneous and evoked activity? Phase-dependence and its relation to the temporal structure of scale-free brain activity. *Cereb Cortex*. <https://doi.org/10.1093/cercor/bhv288>
- Hutt A, Mierau A, Lefebvre J (2016) Dynamic control of synchronous activity in networks of spiking neurons. *PLoS ONE*. <https://doi.org/10.1371/journal.pone.0161488>
- Hwang K, Ghuman AS, Manoach DS, Jones SR, Luna B (2014) Cortical neurodynamics of inhibitory control. *J Neurosci*. <https://doi.org/10.1523/JNEUROSCI.4889-13.2014>
- Hyvärinen A, Oja E (2000) Independent component analysis: algorithms and applications. *Neural Netw*. [https://doi.org/10.1016/S0893-6080\(00\)00026-5](https://doi.org/10.1016/S0893-6080(00)00026-5)
- Irrmischer M, Poil SS, Mansvelder HD, Intra FS, Linkenkaer-Hansen K (2018) Strong long-range temporal correlations of beta/gamma oscillations are associated with poor sustained visual attention performance. *Eur J Neurosci*. <https://doi.org/10.1111/ejn.13672>
- Jansen BH, Rit VG (1995) Electroencephalogram and visual evoked potential generation in a mathematical model of coupled cortical columns. *BiolCybern*. <https://doi.org/10.1007/BF00199471>
- Kanai R, Rees G (2011) The structural basis of inter-individual differences in human behaviour and cognition. *Nat Rev Neurosci*. <https://doi.org/10.1038/nrn3000>
- Khanna P, Carmena JM (2017) Beta band oscillations in motor cortex reflect neural population signals that delay movement onset. *ELife*. <https://doi.org/10.7554/eLife.24573>
- Klimesch W, Sauseng P, Hanslmayr S (2007) EEG alpha oscillations: the inhibition-timing hypothesis. *Brain Res Rev*. <https://doi.org/10.1016/j.brainresrev.2006.06.003>
- Lange J, Halacz J, Van Dijk H, Kahlbrock N, Schnitzler A (2012) Fluctuations of prestimulus oscillatory power predict subjective perception of tactile simultaneity. *Cereb Cortex*. <https://doi.org/10.1093/cercor/bhr329>
- Lefebvre J, Hutt A, Frohlich F (2017) Stochastic resonance mediates the state-dependent effect of periodic stimulation on cortical alpha oscillations. *ELife*. <https://doi.org/10.7554/eLife.32054>
- Liebrand M, Kristek J, Tzvi E, Krämer UM (2018) Ready for change: Oscillatory mechanisms of proactive motor control. *PLoS ONE*. <https://doi.org/10.1371/journal.pone.0196855>
- Lin, W.-T. (2015). Visualization of correlation matrix. [https://es.mathworks.com/matlabcentral/fileexchange/48131-visualization-of-correlation-matrix-mycorrplot\\_1-mycorrplot\\_2](https://es.mathworks.com/matlabcentral/fileexchange/48131-visualization-of-correlation-matrix-mycorrplot_1-mycorrplot_2). Accessed 22 Oct 2020
- Lindner B, Longtin A (2006) Comment on "characterization of sub-threshold voltage fluctuations in neuronal membranes," by M. Rudolph and A. Destexhe. *Neural Comput*. <https://doi.org/10.1162/neco.2006.18.8.1896>
- Linkenkaer-Hansen K, Nikouline VV, Palva JM, Ilmoniemi RJ (2001) Long-range temporal correlations and scaling behavior in human brain oscillations. *J Neurosci*. <https://doi.org/10.1523/jneurosci.21-04-01370.2001>
- Linkenkaer-Hansen K, Nikulin VV, Palva S, Ilmoniemi RJ, Palva JM (2004) Prestimulus oscillations enhance psychophysical performance in humans. *J Neurosci*. <https://doi.org/10.1523/JNEUROSCI.2584-04.2004>
- Lopes Da Silva FH, Pijn JP, Velis D, Nijssen PCG (1997) Alpha rhythms: Noise, dynamics and models. *Int J Psychophysiol*. [https://doi.org/10.1016/S0167-8760\(97\)00767-8](https://doi.org/10.1016/S0167-8760(97)00767-8)
- Maier JX, Ghazanfar AA (2007) Looming biases in monkey auditory cortex. *J Neurosci*. <https://doi.org/10.1523/JNEUROSCI.0330-07.2007>
- Mantini D, Perrucci MG, Cugini S, Ferretti A, Romani GL, Del Gratta C (2007) Complete artifact removal for EEG recorded during continuous fMRI using independent component analysis. *Neuroimage*. <https://doi.org/10.1016/j.neuroimage.2006.09.037>
- Marder E (2011) Variability, compensation, and modulation in neurons and circuits. *Proc Natl Acad Sci USA*. <https://doi.org/10.1073/pnas.1010674108>
- Maris E, Oostenveld R (2007) Nonparametric statistical testing of EEG- and MEG-data. *J Neurosci Methods*. <https://doi.org/10.1016/j.jneumeth.2007.03.024>
- Martens S, Munneke J, Smid H, Johnson A (2006) Quick minds don't blink: electrophysiological correlates of individual differences in attentional selection. *J Cogn Neurosci*. <https://doi.org/10.1162/jocn.2006.18.9.1423>

- Mueller S, Wang D, Fox MD, Yeo BTT, Sepulcre J, Sabuncu MR, Shafee R, Lu J, Liu H (2013) Individual variability in functional connectivity architecture of the human brain. *Neuron*. <https://doi.org/10.1016/j.neuron.2012.12.028>
- Murray JD, Bernacchia A, Freedman DJ, Romo R, Wallis JD, Cai X, Padoa-Schioppa C, Pasternak T, Seo H, Lee D, Wang XJ (2014) A hierarchy of intrinsic timescales across primate cortex. *Nat Neurosci*. <https://doi.org/10.1038/nn.3862>
- Nielsen CS, Stubhaug A, Price DD, Vassend O, Czajkowski N, Harris JR (2008) Individual differences in pain sensitivity: Genetic and environmental contributions. *Pain*. <https://doi.org/10.1016/j.pain.2007.06.008>
- Nunez PL (2000) Toward a quantitative description of large-scale neocortical dynamic function and EEG. *Behav Brain Sci*. <https://doi.org/10.1017/S0140525X00003253>
- Palva JM, Zhigalov A, Hirvonen J, Korhonen O, Linkenkaer-Hansen K, Palva S (2013) Neuronal long-range temporal correlations and avalanche dynamics are correlated with behavioral scaling laws. *Proc Natl Acad Sci USA*. <https://doi.org/10.1073/pnas.1216855110>
- Ploran EJ, Nelson SM, Velanova K, Donaldson DI, Petersen SE, Wheeler ME (2007) Evidence accumulation and the moment of recognition: dissociating perceptual recognition processes using fMRI. *J Neurosci*. <https://doi.org/10.1523/JNEUROSCI.3522-07.2007>
- Saka M (2010) Linear superposition of sensory-evoked and ongoing cortical hemodynamics. *Front Neuroenerg*. <https://doi.org/10.3389/fnene.2010.00023>
- Saka M, Berwick J, Jones M (2012) Inter-trial variability in sensory-evoked cortical hemodynamic responses: the role of the magnitude of pre-stimulus fluctuations. *Front Neuroenerg*. <https://doi.org/10.3389/fnene.2012.00010>
- San Cristóbal B, Vicente R, Sancho JM, Garcia-Ojalvo J (2013) Emergent bimodal firing patterns implement different encoding strategies during gamma-band oscillations. *Front Comput Neurosci*. <https://doi.org/10.3389/fncom.2013.00018>
- Seifritz E, Neuhoff JG, Bilecen D, Scheffler K, Mustovic H, Schächinger H, Elefante R, Di Salle F (2002) Neural processing of auditory looming in the human brain. *Curr Biol*. [https://doi.org/10.1016/S0960-9822\(02\)01356-8](https://doi.org/10.1016/S0960-9822(02)01356-8)
- Smit DJA, Linkenkaer-Hansen K, de Geus EJC (2013) Long-range temporal correlations in resting-state alpha oscillations predict human timing-error dynamics. *J Neurosci*. <https://doi.org/10.1523/JNEUROSCI.2816-12.2013>
- Thomson DJ (1982) Spectrum estimation and harmonic analysis. *Proc IEEE*. <https://doi.org/10.1109/PROC.1982.12433>
- Thut G, Nietzel A, Brandt SA, Pascual-Leone A (2006)  $\alpha$ -Band electroencephalographic activity over occipital cortex indexes visuospatial attention bias and predicts visual target detection. *J Neurosci*. <https://doi.org/10.1523/JNEUROSCI.0875-06.2006>
- Tsuchiya N, Wilke M, Frässle S, Lamme VAF (2015) No-report paradigms: extracting the true neural correlates of consciousness. *Trends Cogn Sci*. <https://doi.org/10.1016/j.tics.2015.10.002>
- Uhlenbeck GE, Ornstein LS (1930) On the theory of the Brownian motion. *Phys Rev*. <https://doi.org/10.1103/PhysRev.36.823>
- Vanderperren K, De Vos M, Ramautar JR, Novitskiy N, Mennes M, Assecondi S, Vanrumste B, Stiers P, Van den Bergh BRH, Wagemans J, Lagae L, Sunaert S, Van Huffel S (2010) Removal of BCG artifacts from EEG recordings inside the MR scanner: a comparison of methodological and validation-related aspects. *Neuroimage*. <https://doi.org/10.1016/j.neuroimage.2010.01.010>
- Wark B, Lundstrom BN, Fairhall A (2007) Sensory adaptation. *Curr Opin Neurobiol*. <https://doi.org/10.1016/j.conb.2007.07.001>
- Werkle-Bergner M, Grandy TH, Chicherio C, Schmiedek F, Lövdén M, Lindenberger U (2014) Coordinated within-trial dynamics of low-frequency neural rhythms controls evidence accumulation. *J Neurosci*. <https://doi.org/10.1523/JNEUROSCI.3801-13.2014>
- Wright JJ, Kydd RR, Sergejew AA (1990) Autoregression models of EEG—results compared with expectations for a multilinear near-equilibrium biophysical process. *Biol Cybern*. <https://doi.org/10.1007/BF00198095>
- Xing D, Shen Y, Burns S, Yeh Ch I, Shapley R, Li W (2012) Stochastic generation of gamma-band activity in primary visual cortex of awake and anesthetized monkeys. *J Neurosci*. <https://doi.org/10.1523/JNEUROSCI.5644-11.2012>

**Publisher's Note** Springer Nature remains neutral with regard to jurisdictional claims in published maps and institutional affiliations.